

Transient Corotating Clumps Around Adolescent Low-Mass Stars From Four Years of TESS

LUKE G. BOUMA,^{1,*} RAHUL JAYARAMAN,² SAUL RAPPAPORT,² LUISA M. REBULL,¹ ALEXANDRE DAVID-URAZ,^{3,4}
LYNNE A. HILLENBRAND,¹ JOSHUA N. WINN,⁵ AND GÁSPÁR Á. BAKOS⁵

¹Department of Astronomy, MC 249-17, California Institute of Technology, Pasadena, CA 91125, USA

²MIT Kavli Institute and Department of Physics, 77 Massachusetts Avenue, Cambridge, MA 02139

³Department of Physics and Astronomy, Howard University, Washington DC, 20059

⁴Center for Research and Exploration in Space Science and Technology, and X-ray Astrophysics Laboratory, NASA/GSFC, Greenbelt, MD 20771, USA

⁵Department of Astrophysical Sciences, Princeton University, 4 Ivy Lane, Princeton, NJ 08540, USA

(Received —; Revised —; Accepted —)

ABSTRACT

We study a set of pre-main-sequence stars with sub-solar masses, rotation periods of 0.2–2 days, optical variability amplitudes of a few percent, and sharp recurring light curve features that last for hundreds of cycles. The sharp features are probably caused by eclipsing clumps of dust or gas orbiting at the corotation radius. We refer to this class of variable star as “complex rotators” (CRs). To improve our understanding of these enigmatic objects, we conducted a survey for CRs using TESS short-cadence data collected between 2018 July and 2022 September. Our search of 65,760 K and M dwarfs with $T < 16$ and $d < 150$ pc yielded 50 high-quality CRs, most of which are new discoveries. Our sample includes the brightest ($T \approx 9.5$), closest ($d \approx 20$ pc), and oldest (≈ 200 Myr) known CRs. One of the new discoveries, LP 12-502, stands out for the complexity of its light curve — with as many as eight flux dips per cycle — and the detail with which the evolution in each dip’s amplitude and phase can be tracked over 1,500 cycles. We argue that corotating gas or dust remains the most viable explanation for CRs. The gas or dust is probably entrained by the star’s magnetic field, and the sharp features may result from a multipolar field topology, a hypothesis supported by correspondences between the light curves of CRs and of B stars known to have strong multipolar magnetic fields.

Keywords: Weak-line T Tauri stars (1795), Periodic variable stars (1213), Circumstellar matter (241), Star clusters (1567), Stellar magnetic fields (1610), Stellar rotation (1629)

1. INTRODUCTION

All young stars vary in optical brightness, and the origin of such variability is, in most cases, understood. Well-explored sources of optical variability include inhomogeneities on stellar surfaces such as starspots and faculae (e.g. Basri 2021), occultations by circumstellar disks (e.g. Bodman et al. 2017), and, in geometrically favorable circumstances, eclipses by stars and planets (e.g. Rizzuto et al. 2020). More exotic sources of optical variability that are potentially relevant to this work include transiting exocomets (e.g. β Pic; Zieba et al. 2019), disintegrating rocky bodies (e.g. KOI-2700; Rappaport et al. 2014), and occultations by circumstellar plasma clumps (e.g. σ Ori E; Townsend et al. 2005; Townsend & Owocki 2005).

Data from K2 (Howell et al. 2014) and TESS (Ricker et al. 2015) have revealed a new class of variable star for which

the root cause of variability is only beginning to become clear: complex rotators (CRs). These objects are identified from their optical light curves, which show nearly periodic troughs that are either sharp or broad; these troughs are often superposed on quasi-sinusoidal spot-like modulation (Stauffer et al. 2017, 2018; Zhan et al. 2019). Some CRs show up to eight dips per cycle. Most CRs are pre-main-sequence M dwarfs with ages of $\approx 5\text{--}150$ million years (Myr), and rotation periods of 0.2–2 days. They are observed to comprise $\approx 1\text{--}3\%$ of M dwarfs younger than 100 Myr (Rebull et al. 2016; Günther et al. 2022). They generally do not show near-infrared excesses indicative of dusty disks, but the wavelength-dependent dip amplitudes of some CRs is consistent with reddening by dust (Onitsuka et al. 2017; Bouma et al. 2020; Günther et al. 2022; Koen 2023). The dip amplitudes and phases usually evolve gradually over tens to hundreds of cycles, although they have occasionally been observed to change abruptly within one cycle (e.g. Stauffer et al. 2017; Palumbo et al. 2022; Popinchalk et al. 2023).

The sharp features of CR light curves can have durations as short as 5% of the rotation period (P_{rot}), which is too short to be caused by starspots rotating into and out of view. Starspots

Corresponding author: Luke G. Bouma

luke@astro.caltech.edu

* 51 Pegasi b Fellow



Figure 1. Complex rotators (CRs): *Top:* Phase-folded TESS light curves for three CRs. Each panel shows the average of the data accumulated over one month, relative to the mean stellar brightness. Gray circles are raw 2-minute data; black circles are binned to 300 points per cycle. The period in hours is printed in the bottom right corner. Left-to-right, the objects are LP 12-502 (TIC 402980664; Sector 19), TIC 94088626 (Sector 10), and TIC 425933644 (Sector 28). *Bottom:* Cartoon explanations for the phenomenon. The dust clump scenario (left) and gas prominence scenario (right) both invoke magnetically-entrained corotating material.

produce flux variations with characteristic timescales of P_{rot} and $0.5P_{\text{rot}}$. With finely-tuned viewing geometries, starspots can produce dip durations as short as $\approx 0.2P_{\text{rot}}$, but in such cases, limb darkening causes the dip amplitudes to be smaller than the observed amplitudes of $\sim 1\%$ (see Stauffer et al. 2017, Figures 37-41). Thus, a “starspot-only” scenario can be ruled out for many CRs (Stauffer et al. 2017; Zhan et al. 2019; Koen 2021). Given that many CRs cannot be explained by starspots alone, and working under the assumption that all CRs share the same basic physical scenario, we discard the “starspot-only” scenario. Instead, the correct explanation probably involves material above the stellar surface that is spatially confined with sharp boundaries (e.g. Stauffer et al. 2017; Günther et al. 2022).

Figure 1 illustrates two proposed models for the extrinsic material. The first scenario invokes opaque dust “clumps” that orbit near the Keplerian corotation radius [$R_c = (GM/\Omega^2)^{1/3}$, where $\Omega = 2\pi/P_{\text{rot}}$] and periodically transit the star (Stauffer et al. 2017; Sanderson et al. 2023). The second scenario invokes “prominences”, long-lived condensations of cool, dense, marginally-ionized gas that are embedded within the hotter corona and that corotate with the star (Collier Cameron & Robinson 1989; Jardine & Collier Cameron 2019; Waugh & Jardine 2022). These hypothetical prominences are analogous to quiescent prominences and filaments seen in the solar corona (see e.g. Vial & Engvold 2015), though rather than existing at a fraction of the stellar radius as in the solar case, they would exist at distances of a

few stellar radii. A final possibility is that an optically-thick ring obscures a narrow band of the stellar photosphere (Zhan et al. 2019). Hot spots passing behind such a ring could produce sudden dips. We do not favor this scenario (see Appendix A).

The dust clump and gas prominence hypotheses are geometrically similar; one could imagine dust or gas accumulating in either of the geometries shown in Figure 1. The main distinguishing factor between the two models is the composition of the occulting material. “Dust clumps” invoke opacity from dust, which would need to be collisionally charged (Sanderson et al. 2023). “Gas prominences” invoke opacity from partially-ionized gas, likely bound-free transitions in hydrogen or perhaps a molecular opacity. Unambiguous evidence in support of either scenario has yet to be acquired. Such evidence might include a spectroscopic detection of silicate $10\text{ }\mu\text{m}$ dust absorption during a dip, or perhaps detection of transient Balmer-line excesses as a function of cycle phase, similar to observations made in systems such as AB Dor (see Collier Cameron 1999) or PTFO 8-8695 (Johns-Krull et al. 2016).

In both models, the corotation radius is the location at which matter concentrates. The empirical basis for this is that the sharp CR features are superposed over smooth, quasi-sinusoidal starspot profiles. The theoretical importance of the corotation radius has been discussed in studies of magnetic rotators (e.g. Lamb et al. 1973; Nakajima 1985; Long et al. 2005). In regions where the magnetic field dominates the

flow (i.e. $B^2/8\pi > \rho v^2/2$), matter is dragged along with the field lines. The tendency for charged gas or dust to become trapped at corotation is then tied to how of the four relevant forces – gravity, Lorentz, inertial Coriolis, and inertial centrifugal – the Lorentz and Coriolis only act perpendicular to field lines, while gravity and the centrifugal force are in balance at R_c (e.g. Townsend & Owocki 2005, their Section 2). Another way to phrase this statement is that there is a local minimum in the effective potential of the corotating frame; given a flow from either the star or from a tenuous accretion disk, this local potential minimum enables material to build up (Townsend & Owocki 2005).

Although theoretical heritage for understanding rapid magnetic rotators exists, CRs have remained mysterious because they have been both hard to discover and hard to characterize. They are hard to discover because they are rare: CRs comprise $\approx 1\%$ of the youngest $\approx 1\%$ of M dwarfs (Rebull et al. 2018). Out of the millions of stars monitored by K2 and TESS, about 50 CRs have been reported to date (Rebull et al. 2016; Stauffer et al. 2017, 2018; Zhan et al. 2019; Bouma et al. 2020; Günther et al. 2022; Popinchalk et al. 2023). They have been hard to characterize because many of the known CRs are relatively faint; the initial K2 discoveries (Rebull et al. 2016; Stauffer et al. 2017) were M2-M6 dwarfs at distances $\gtrsim 100$ pc, yielding optical brightnesses of $V \approx 15.5$ to $V > 20$. At such magnitudes, high-resolution time-series spectroscopy is out of reach with current facilities, despite the potential utility of such observations.

In this work, we aim to find bright and nearby CRs, since these objects will be the most amenable to detailed photometric and spectroscopic analyses. To do this, we use 120-second cadence data acquired by TESS between 2018 July and 2022 September (Sectors 1-55; Cycles 1-4). We present our search methods in Section 2, and the resulting CR catalog in Section 3. The observed evolution of many CRs over a two-year baseline is described in Section 4, including a deep-dive into the behavior of an especially interesting object, LP 12-502. We discuss a few implications in Section 5, and conclude in Section 6.

Some comments on nomenclature are needed. What we are calling “complex rotators” (Zhan et al. 2019; Günther et al. 2022; Popinchalk et al. 2023) have also been called “transient flux dips”, “persistent flux dips”, and “scallop shells” by Stauffer et al. (2017), or more generally “complex periodic variables” by Koen (2023). The CRs should not be conflated with “dippers”, which are classical T Tauri stars with infrared excesses, and which show large-amplitude variability linked to obscuring inner disk structures and accretion hot spots (Cody et al. 2014; Robinson et al. 2021). The phenomenology and stellar properties of CRs and dippers are quite different (though see Sections 3.3 and 5.7). While we considered other possibilities, we ultimately concluded that “complex rotator” correctly draws attention to the fact that rotation will play a fundamental role in explaining these objects, and that their key defining feature is the complexity of their optical light curves relative to the quasi-sinusoidal modulations of starspots.

2. METHODS

2.1. Stellar selection function

To construct our sample, we analyzed the short-cadence data acquired by TESS between 2018 July 25 and 2022 September 1 (Sectors 1-55). Specifically, we used the 120-second cadence light curves produced by the Science Processing and Operations Center at the NASA Ames Research Center (Jenkins et al. 2016). While the TESS data products from these sectors also included full frame images with cadences of 600 and 1800 seconds for a larger number of sources, we restricted our attention to the 120-second data for the sake of uniformity and simplicity in data handling. In exchange, we sacrificed both completeness and homogeneity of the selection function. While TESS cumulatively observed $\approx 90\%$ of the sky for at least one lunar month between 2018 July and 2022 September, the 120-second cadence data were collected for only a subset of observable stars that were preferentially nearby and bright (see Fausnaugh et al. 2021). The total 120-second data volume from Sectors 1-55 included 1,087,475 short-cadence light curves, which were available for 428,121 unique stars.

To further simplify our search, we defined our target sample as stars with 120-second cadence TESS light curves satisfying the following four conditions:

$$T < 16 \quad (\text{Amenable with TESS}) \quad (1)$$

$$G_{\text{BP}} - G_{\text{RP}} > 1.5 \quad (\text{Red stars only}) \quad (2)$$

$$M_G > 4 \quad (\text{Dwarf stars only}) \quad (3)$$

$$d < 150 \text{ pc} \quad (\text{Close stars only}) \quad (4)$$

Here, $M_G = G + 5 \log(\varpi_{\text{as}}) + 5$ is the Gaia G -band absolute magnitude, ϖ_{as} is the parallax in units of arcseconds, and d is a geometric distance defined by inverting the parallax and ignoring any zero-point correction. We performed this selection by cross-matching TIC8.2 (Stassun et al. 2019; Paegert et al. 2021) against the Gaia DR2 point-source catalog (Gaia Collaboration et al. 2018). We opted for Gaia DR2 rather than DR3 because the base catalog for TIC8 was Gaia DR2, which facilitated a one-to-one crossmatch using the Gaia source identifiers. The target sample ultimately included 65,760 M dwarfs and late-K dwarfs, down to $T < 16$ and out to $d < 150$ pc. For stars with multiple sectors of TESS data available, we searched for CR signals independently. In total, our 65,760 star target list included 180,017 month-long light curves.

We assessed the completeness of our selection function by comparing the number of stars with TESS Sector 1-55 short-cadence data against the number of Gaia DR2 point sources. We required all stars to meet conditions 1-4. The results are shown in Figure 2. TESS 2-minute data exist for $\approx 50\%$ of $T < 16$ M and late-K dwarfs at ≈ 50 pc. Within 20 pc, $\gtrsim 80\%$ of the $T < 16$ M and late-K dwarfs have at least one sector of short-cadence data. Beyond 100 pc, $\lesssim 10\%$ of such stars have any short-cadence data available. This can be translated into our sensitivity for the lowest mass stars by considering



Figure 2. Completeness of the TESS 2-minute data for late-K and early M dwarfs near the Sun, from Sectors 1-55. The orange dotted curve shows the number of stars in successive radial shells, each with a width of 10 pc. To be part of our selection function, these stars must meet the listed conditions: they must be red dwarf stars ($G_{\text{BP}} - G_{\text{RP}} > 1.5$; $M_G > 4$) amenable for TESS observations ($T < 16$). The blue solid curve shows the fraction of such stars with at least one sector of TESS 2-minute cadence data acquired between Sectors 1-55.

that the spectral type of a $T=16$ star at $d=50$ pc is $\approx \text{M}5.5\text{V}$, corresponding to a main-sequence mass of $\approx 0.12 M_\odot$.

2.2. CR discovery

Prior to this study, most CRs have been found by visually examining all the light curves of stars in young clusters (Rebull et al. 2016; Stauffer et al. 2017; Popinchalk et al. 2023), or by flagging light curves with short periods and a large number of strong Fourier harmonics for visual inspection (Zhan et al. 2019). In this work, we implemented a new search approach based on counting the number of sharp local minima in phase-folded light curves, while also using the Fourier approach. We applied these two search techniques independently.

2.2.1. Counting dips

The dip counting technique aims to count sharp local minima in phase-folded light curves. The most remarkable CRs often show three or more dips per cycle, which distinguishes them from other types of variables such as synchronized and spotted binaries (RS CVn stars).

For our dip-counting pipeline, we began with the PDC_SAP light curves for each sector, removed non-zero quality flags, and normalized the light curve by dividing out its median value. We then flattened the light curve using a 5-day sliding median filter, as implemented in wotan (Hippke et al. 2019). We computed a periodogram of the resulting cleaned and flattened light curve, opting for the Stellingwerf (1978) phase dispersion minimization (PDM) algorithm

implemented in astrobase (Bhatti et al. 2021) due to its shape agnosticism. If a period P below 2 days was identified, we reran the periodogram at a finer grid to improve the accuracy of the period determination.

Once a star’s period was identified, we binned the phased light curve to 100 points per cycle. To separate sharp local minima from smooth spot-induced variability, we then iteratively fit robust penalized splines to the wrapped phase-folded light curve, excluding points more than two standard deviations away from the local continuum (Hippke et al. 2019). The wrapping procedure is discussed below. In this fitting framework, the maximum number of equidistant spline knots per cycle is the parameter that controlled the meaning of “sharp” — we allowed at most 10 such knots per cycle, though for most stars fewer knots were preferred based on cross-validation using an ℓ^2 -norm penalty. An example fit is shown in panel (e) of Figure 3.

We then identified local minima in the resulting residual light curve using the SciPy `find_peaks` utility (Virtanen et al. 2020), which is based on comparing adjacent values in an array. For a peak to be flagged as significant, we required it to have a width of at least $0.02P$, and a height of at least twice the noise level. The noise level was defined as the 68th percentile of the distribution of the residuals from the median value of $\delta f_i \equiv f_i - f_{i+1}$, where f is the flux and i is an index over time. In panel (e) of Figure 3, automatically-identified local minima are shown with the gray triangles.

Wrapping is necessary to eliminate edge effects when fitting the light curve and when identifying local minima in the residuals. A phased light curve would usually cover phases $\phi \in [0, 1]$. We instead performed the analysis described above using a phase-folded light curve spanning $\phi \in [-1, 2]$, which was created by duplicating and concatenating the ordinary phase-folded light curve. The free parameters we adopted throughout the analysis – for instance the maximum number of spline knots per cycle, and the height and depth criteria for dips – were chosen during testing based on the desire to correctly re-identify a large fraction ($> 90\%$) of previously known CRs, while also being able to consistently reject common false positives such as rapidly rotating spot-induced variability and typical eclipsing binaries.

In short, CR candidates were identified by requiring a peak PDM period below two days and the presence of at least three sharp local minima, based on at least one sector of the TESS 120-second data. Candidates were then inspected visually as described in Section 2.2.3.

2.2.2. Fourier analysis

We performed an independent search using a Fourier-based approach, following Zhan et al. (2019) and Pribulla et al. (2023, their Section 1.3). Starting with the PDC_SAP light curves, we normalized each light curve, and then re-binned it into equal width 120-second bins to account for the uneven spacing in the TESS data, as well as the data gap caused by satellite downlink during each sector. We then padded the data to ensure that the light curve had a length that was a power of two, as described by Zhan et al.. After tak-

ing the Fourier transform of the padded light curve using `numpy.fft`, we searched for peaks with a significance exceeding 12σ within a set of 500 frequency bins.

If a peak of such significance was found, we generated a “summary sheet” with information about the star, its full and folded light curves, Fourier transform, potential contaminating stars, and information about these contaminating stars. Summary sheets were generated for $\approx 10\%$ of the 20,000 120-second targets in each sector. We reviewed each summary sheet and tried to classify each light curve based on visual inspection of its morphology (with categories including eclipsing binary, CR, RS CVn, and cataclysmic variable). Whenever a CR was identified, the light curves from multiple sectors were stitched together and analyzed jointly, for a more accurate period determination.

2.2.3. Manual vetting

We assessed whether the objects found using the dip-counting (Section 2.2.1) and Fourier (Section 2.2.2) techniques were consistent with expectations for CRs by assembling the data shown in Figure 3. We labeled a star as a “good” CR if it met all of the following criteria for at least one TESS sector:

- $P < 2$ days.
- At least three dips per cycle, or else otherwise oddly-shaped dips.
- Dip phases (mostly) repeat over ≈ 30 day sector duration.

We also noted “possible” CRs for which the classification was more ambiguous, and “false positives” that are definitely not CRs. The most common false positives for both the Fourier and dip-counting techniques were eclipsing binaries, ordinary spotted rapid rotators, and complex light curves due to multiple stars contributing to the photometric aperture. Our dip-counting pipeline flagged 368 unique stars for visual inspection; about 20% were subsequently labeled either good or possible CRs. From the Fourier pipeline, $\approx 0.5\%$ of stars that passed the 12σ peak threshold were eventually classified as CRs. This is because the Fourier pipeline was implemented as a general variability search; its results are also being used for analyses on topics other than CRs.

2.3. Stellar properties

Ages—We estimated the stellar ages by making probabilistic spatial and kinematic associations between the CRs and known clusters in the solar neighborhood. For most stars in our sample, we did this using BANYAN Σ (Gagné et al. 2018).¹ This algorithm calculates the probability that a given star belongs to one of 27 young clusters (or “associations”) within 150 pc of the Sun, by modeling the clusters as multivariate Gaussian distributions in 3-D position and 3-D velocity space. We used the Gaia DR2 sky positions, proper motions, and distances to calculate the membership probabilities. BANYAN Σ in turn analytically marginalizes over

the radial velocity dimension. The probabilities returned by this procedure are qualitatively useful, but should be interpreted with caution because the assumption of Gaussian distributions is questionable for most groups within the solar neighborhood (see e.g. Kerr et al. 2021, Figure 10).

For a few cases where BANYAN Σ yielded ambiguous results, we consulted the meta-catalog of young, age-dated, and age-dateable stars provided by Bouma et al. (2022), and also searched the local volume around each star for co-moving companions.²

Effective temperatures, radii, and masses—We determined the stellar effective temperature and radii by fitting the broadband spectral energy distributions (SEDs); we then estimated the masses by interpolating against the sizes, temperatures, and ages of the PARSEC v1.2S models (Bressan et al. 2012; Chen et al. 2014).

For the SED fitting, we used `astroARIADNE` (Vines & Jenkins 2022). We adopted the BT-Settl stellar atmosphere models (Allard et al. 2012) assuming the Asplund et al. (2009) solar abundances, and the Barber et al. (2006) water line lists. The broadband magnitudes we considered included $GG_{\text{BP}}G_{\text{RP}}$ from Gaia DR2, $Vgri$ from APASS, JHK_S from 2MASS, SDSS riz , and the WISE $W1$ and $W2$ passbands. We omitted UV flux measurements from our SED fit to avoid any possible bias induced by chromospheric UV excess. We omitted WISE bands $W3$ and $W4$ due to reliability concerns. `astroARIADNE` compares the measured broadband flux measurements against pre-computed model grids, and by default fits for six parameters: $\{T_{\text{eff}}, R_*, A_V, \log g, [\text{Fe}/\text{H}], d\}$. The distance prior is drawn from Bailer-Jones et al. (2021). The surface gravity and metallicity are generally unconstrained. Given our selection criteria for the stars, we assumed the following priors for the temperature, stellar size, and extinction:

$$T_{\text{eff}}/\text{K} \sim \mathcal{N}(3000, 1000), \quad (5)$$

$$R_*/R_{\odot} \sim \mathcal{T}_N(0.5, 0.3, 0.1, 1.5), \quad (6)$$

$$A_V/\text{mag} \sim \mathcal{U}(0, 0.2), \quad (7)$$

for \mathcal{N} the Gaussian and \mathcal{U} the uniform distributions, and $\mathcal{T}(\mu, \sigma, a, b)$ a truncated normal distribution with mean μ , standard deviation σ , and lower and upper bounds a and b . We validated our chosen upper bound on A_V using a 2MASS color-color diagram. Finally, using `Dynesty` (Speagle 2020), we sampled the posterior probability assuming the default Gaussian likelihood, and set a stopping threshold of $d \log \mathcal{Z} < 0.01$, where \mathcal{Z} denotes the evidence.

With the effective temperatures and stellar radii from the SED fit, we estimated the stellar masses by interpolating against the PARSEC isochrones (v1.2S Chen et al. 2014). The need for models that incorporate some form of correction for young, active M dwarfs is well-documented (e.g. Stassun et al. 2012; David & Hillenbrand 2015; Feiden 2016; Somers

¹ https://github.com/jgagneastro/banyan_sigma, git commit 394b486

² <https://github.com/adamkraus/Comove>, git commit 278b372

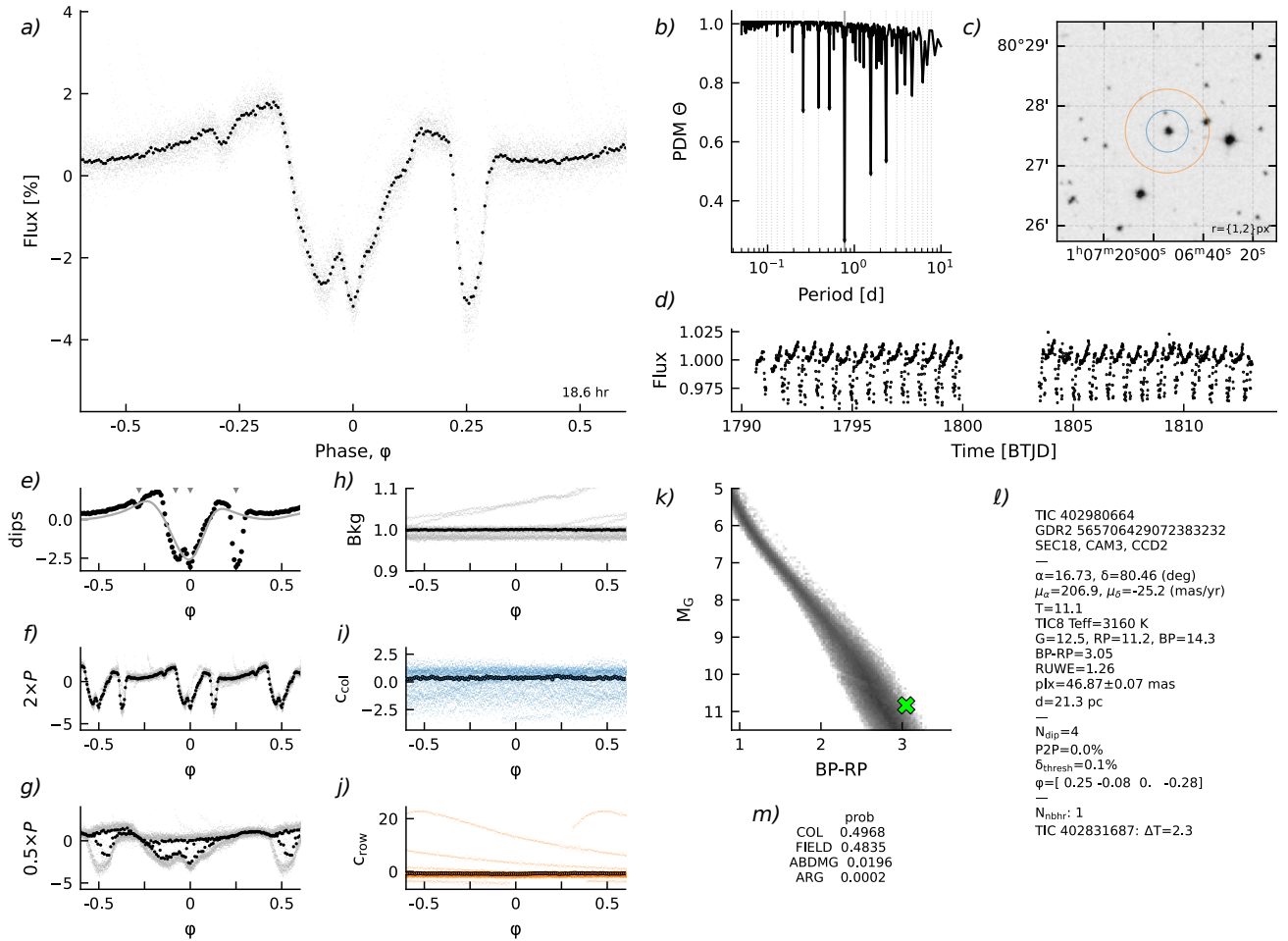


Figure 3. Validation plots used to classify CRs. The complete figure set, with one image per sector for each of the 66 objects in Table 1 is available in the online journal. **For internal collaboration review:** <https://www.dropbox.com/sh/khtwk5a6z0zgrif/AABRG21Ire7VS4BUnaD1hOR8a?dl=0>. Panels are as follows. *a*): Phase-folded light curve; gray points are raw 2-minute data and black points are binned to 200 points per cycle. The adopted period is given in the lower-right corner. *b*): Phase-dispersion minimization (PDM) periodogram. Dotted lines show up to the 10th harmonic and subharmonic. *c*): DSS finder chart, with 21'' and 42'' radius circles for scale. One TESS pixel has a full side length of 21''. *d*): Cleaned light curve, binned to 20-minute cadence, in Barycentric TESS Julian Date (BTJD). *e*): Phase-folded light curve, binned to 100 points per cycle. The gray line denotes the spline-fit to the wrapped phase-folded light curve, and small gray triangles denote automatically identified local minima. *f*): Phase-folded light curve at twice the peak period. *g*): Phase-folded light curve at half the peak period. *h*): Phase-folded time-series within the “background” aperture defined in the SPOC light curves. *i*): Phase-folded flux-weighted centroid in the column direction. *j*): Phase-folded flux-weighted centroid in the row direction. *k*): Gaia DR2 color–absolute magnitude diagram. The gray background denotes stars within 100 pc from [Gaia Collaboration et al. \(2021\)](#). *l*): Information from Gaia DR2, TIC8, and the automated dip-counting search pipeline. “Neighbors”, abbreviated “nbhr”, are listed within apparent distances of 2 TESS pixels if $\Delta T < 2.5$. *m*): BANYAN- Σ v1.2 association probabilities, calculated using positions, proper motions, and the parallax.

et al. 2020). Plausible explanations for the disagreement between observed and theoretical M dwarf colors and sizes include starspot coverage (e.g. Gully-Santiago et al. 2017) and potentially incomplete line lists (e.g. Rajpurohit et al. 2013). In the PARSEC models, Chen et al. (2014) performed an empirical correction to the temperature–opacity relation drawn from the BT-Settl model atmospheres, in order to match observed masses and radii of young eclipsing binaries. This is sufficient for our goal of estimating stellar masses. Given our estimates of $\{\tilde{T}_{\text{eff}}, \tilde{M}_*, \tilde{t}\}$, and approximating their uncertain-

ties as Gaussian $\sigma_{\tilde{T}_{\text{eff}}}$, $\sigma_{\tilde{M}_*}$ and $\sigma_{\tilde{t}}$, we define a distance metric Δ to each model PARSEC grid-point $\{T_{\text{eff}}, M_*, t\}$ via

$$\Delta^2 = \left(\frac{\tilde{T}_{\text{eff}} - T_{\text{eff}}}{\sigma_{\tilde{T}_{\text{eff}}}} \right)^2 + \left(\frac{\tilde{M}_* - M_*}{\sigma_{\tilde{M}_*}} \right)^2 + \left(\frac{\tilde{t} - t}{\sigma_{\tilde{t}}} \right)^2, \quad (8)$$

where the division by the uncertainties helps to assign equal importance to each dimension. The mass reported in Table 1 is the model mass that minimizes the distance. The reported uncertainties in the masses are based on propagating the statistical uncertainties in the radii, temperatures, and ages.

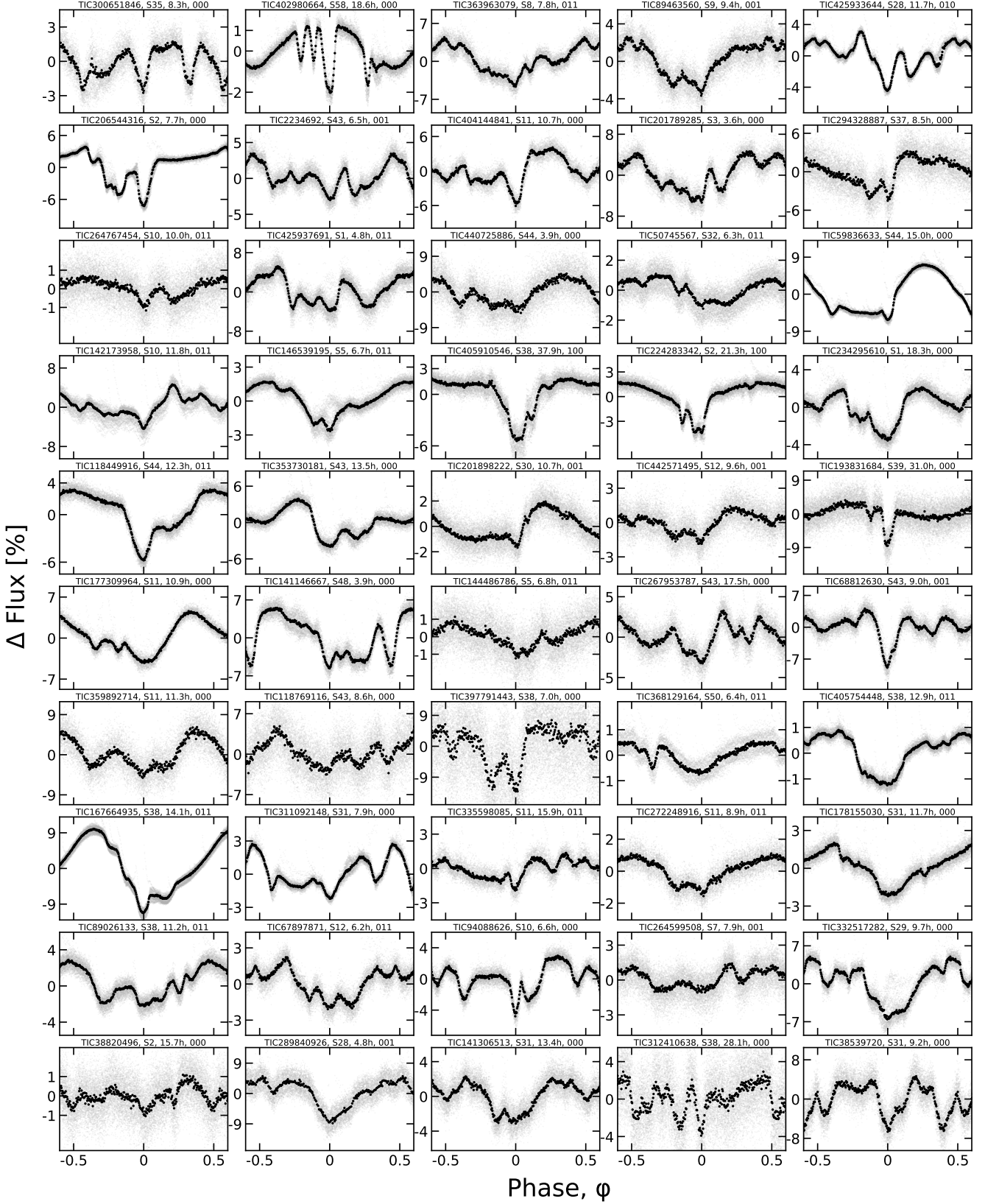


Figure 4. CRs found in the TESS 2-minute data. Phased TESS light curves over one month are shown for 50 CRs in the high quality sample. Gray are raw 2-minute data; black bins to 300 points per cycle. Objects are ordered such that sources with the most TESS data available are on top (see Section 3.1). Zero phase is chosen to correspond to minimum light. Each panel is labeled by the TIC identifier, the TESS sector number, the period in hours, and the three-bit binarity flag from Table 1, which denotes Gaia DR3 `radial_velocity_error` outliers (bit 1), Gaia DR3 `ruwe` outliers (bit 2), and stars with secondary TESS periods (bit 3).

3. RESULTS

3.1. CR catalog

Table 1 lists the 66 objects identified by our search. The 50 stars in the “good” sample demonstrated what we deemed to be the key characteristics of the CR phenomenon in at least one TESS sector. The classification of 13 CR candidates was ambiguous, and the 3 remaining objects were notable false positives that we discuss below. The quality column in the table divides the three classes; additional data from TESS or other instruments could help resolve the classification of the ambiguous cases. Of the 63 CRs and candidate CRs, 32 were found using both the dip-counting and Fourier techniques, 23 were found using only the dip-counting technique, and 8 were found using only the Fourier technique. In the following, we will focus our discussion on the good sample, irrespective of discovery method. We will often refer to stars by their TIC identifiers; the easiest way to reference these against the figures in most document readers is to use a “find” ($\text{Ctrl}+\text{F}$) utility.

Figure 4 is a mosaic of phased light curves for the 50 CRs. The objects are sorted first in order of the number of TESS 120-second cadence sectors in which they clearly demonstrated the CR phenomenon, and secondarily by descending brightness. The top five objects by this metric are TIC 300651846 ($T=13.5$, 12 sectors); TIC 402980664 ($T=11.1$, 7 sectors); TIC 89463560 ($T=13.5$, 5 sectors); TIC 363963079 ($T=12.9$, 5 sectors); and TIC 294328887 ($T=14.2$, 4 sectors). The brightest five CRs span $9.3 < T < 11.1$; the faintest five span $14.5 < T < 15.0$. The fastest five have periods spanning $3.6 \text{ hr} < P < 6.2 \text{ hr}$, and the slowest five span $27 \text{ hr} < P < 38 \text{ hr}$.

The light curves show between two and eight local minima per cycle. Some stars show ordinary sinusoidal modulation during one portion of the phased light curve, and highly structured modulation in the remainder of the cycle (e.g. TIC 206544316, TIC 224283342, TIC 402980664). Others show structured modulation over the entire span of a cycle (e.g. TIC 2234692, TIC 425933644, TIC 142173958). Others show some mix between these two modes.

A small number of objects at first glance seem reminiscent of eclipsing binaries, such as TIC 193831684, TIC 59836633, or TIC 5714469. We believe these cases are unlikely to be eclipsing binaries due to the additional coherent peaks and troughs in the light curves, which are distinct from any binary phenomena of which we are aware.

3.2. Ages

Of our 63 confirmed and candidate CRs, 61 were associated with a nearby moving group or open cluster, primarily using BANYAN Σ .³ The relevant groups are listed in Table 1; their ages span $\approx 5\text{-}200$ Myr. The groups that contain

the largest number of CRs in our catalog are Sco-Cen, Tuc-Hor, and Columba. Six CRs were also identified in the Argus association (Zuckerman 2019), which serves as an indirect line of evidence supporting the reality and youth of that group. The large contribution from Sco-Cen is not surprising since Sco-Cen contains the majority of pre-main-sequence stars in the solar neighborhood, and many of its stars were selected for TESS 120-second cadence observations by guest investigators. Given the $\lesssim 10\%$ completeness of TESS beyond 100 pc, there may be many more CRs in Sco-Cen that remain to be discovered.

There were two stars for which neither BANYAN Σ nor a literature search led to a confident association with any young group. Both stars display CR signals over multiple TESS sectors. Both are photometrically elevated relative to the main sequence, an indication of youth. Both were also noted by Kerr et al. (2021) as being in the “diffuse” population of < 50 Myr stars near the Sun.

Our search confirms that the CR phenomenon persists for at least ≈ 150 Myr. Table 1 includes three ≈ 150 Myr CRs in AB Dor (Bell et al. 2015), a ≈ 112 Myr old Pleiades CR (Dahm 2015), and a similarly-aged Psc-Eri member (Ratzenböck et al. 2020). To our knowledge, TIC 332517282 in AB Dor ($t=149^{+51}_{-19}$ Myr; Bell et al. 2015) was the previous record-holder for the oldest-known CR (Zhan et al. 2019; Günther et al. 2022); at least one unambiguous CR (EPIC 211070495) and a few other candidates were also previously known in the Pleiades (Rebull et al. 2016).

The maximum age of CRs might even exceed 200 Myr, based on the candidate membership of TIC 294328887 in the Carina Near moving group (Zuckerman et al. 2006). The estimated age of this group, 200 ± 50 Myr, is based on the lithium sequence of its G-dwarfs (Zuckerman et al. 2006), which shows a coeval population of stars older than the Pleiades and younger than the 400 Myr Ursa Major moving group. However, the formal BANYAN- Σ membership probability is somewhat low (only 6%), perhaps due to the missing radial velocity. This lack of information could be rectified by acquiring even a medium-resolution spectrum. An independent assessment of the group’s kinematics using Gaia data, and its rotation sequence using TESS, could also bear on the question of whether TIC 294328887 is a member.

3.3. Infrared excesses

Most CRs in our catalog did not show infrared excesses in the $W1\text{-}W4$ bands, which is typical for this class of object (Stauffer et al. 2017). Visually inspecting the SEDs of our 66 star sample and the WISE images available through IRSA, we labeled two objects as having reliable infrared excesses (both $W3$ and $W4$ fluxes are more than 3σ above the photospheric prediction): TIC 193136669 (TWA 34) and TIC 57830249 (TWA 33).

Both of these stars with IR excesses are in the TW Hydreae association (≈ 10 Myr). They have periods of 38 hr and 44 hr, respectively. In our initial labeling, we labeled both as “ambiguous” CRs because the dips in their Sector 36 light curves seemed to stochastically evolve over only one or a few cycles,

³ Two of the 61 memberships were made with low confidence and are flagged in Table 1. The assignment of TIC 397791443 to IC 2602 was based not on BANYAN Σ but instead on a literature search (e.g. Cantat-Gaudin & Anders 2020).

which is not typical of CRs; their periods were also long in comparison with most of the other CRs. Inspection of additional sectors clarified that both sources are dippers, not CRs (see the online plots in Figure 3). For TIC 57830249, the Sector 10 light curve shows completely different behavior from Sector 36, with variability amplitudes of $\pm 50\%$ and no obvious periodicity. TIC 57830249 also shows continuum emission at 1.3 mm (Rodriguez et al. 2015), which suggests that cold dust grains are present.

The dipper classification of TIC 193136669 is less obvious; the main indication that it is a dipper is that Sectors 62 and 63 show its dips appearing and disappearing within the span of one cycle. None of the CRs in our sample exhibit this property. Independently, TIC 193136669 is known to have a cold disk of dust and molecular gas, based on 1.3 mm continuum emission and resolved $^{12}\text{CO}(2-1)$ emission (Rodriguez et al. 2015). It was labeled a dipper by Capistrant et al. (2022); we agree with their designation, and label it an “impostor” CR in Table 1. Section 5.7 highlights plausible evolutionary connections between CRs and dippers in light of these “misclassifications”.

3.4. Binarity

The main types of binaries of interest in this work were those that were unresolved, because they can lead to misinterpretations of the data. For instance, unresolved binaries might produce multiple photometric signals and hinder our ability to correctly identify the star hosting the CR signal. Unresolved binaries could also bias photometric magnitude and color measurements, which would affect our stellar parameter estimates. To attempt to identify binaries, we considered the following lines of information.

Radial velocity scatter—We examined diagrams of the Gaia DR3 “radial velocity error” as a function of stellar color for all 63 CRs and candidate CRs. Since this quantity represents the standard deviation of the non-published Gaia RV time series, outliers can suggest single-lined spectroscopic binarity. These plots showed two clusters of stars, at $\lesssim 10 \text{ km s}^{-1}$ and $20\text{-}25 \text{ km s}^{-1}$. We therefore adopted a threshold of 20 km s^{-1} to flag possible single-lined spectroscopic binaries, which selected three stars: TIC 405910546, TIC 224283342, and TIC 280945693.

RUWE—We examined plots of Gaia DR3 RUWE as a function of color.⁴ Elevated RUWEs imply excess astrometric noise relative to a single-source model. This can be caused by marginally resolved binaries, intrinsic photometric variability, or intrinsic astrometric motion. Based on this exercise, we adopted a threshold of $\text{RUWE}_{\text{DR3}} > 2$ to flag sources with excess astrometric noise. This threshold was met by 16/50 high-quality CRs and by 0/13 of the ambiguous CRs. The choice of the threshold RUWE is somewhat subjective, since the RUWE distribution has an extended tail (e.g.

Penoyre et al. 2022). If we had instead required $\text{RUWE}_{\text{DR3}} > 1.4$, 21/50 high-quality CRs and 2/13 of the ambiguous sample would have been flagged.

Gaia DR3 non-single stars—Gaia DR3 included a `non_single_star` column that flagged eclipsing, astrometric, and spectroscopic binaries. None of the stars in our CR sample were identified as possible binaries in this column.

Multiple periodic TESS signals—During our visual analysis of the TESS light curves and PDM periodograms, we flagged sources with beating light curves, and with PDM periodograms that showed multiple periods. We also attempted to disentangle the two signals by subtracting the mean CR signal over each sector, and then repeating the phase-dispersion minimization analysis. The results of this effort are summarized in the secondary periods, P_{sec} , listed in Table 1, which we required to be at least 5% different from the primary period. This process yielded 22/50 high-quality CRs with secondary periods; 3/13 of the ambiguous sample met the same criterion. Of the 16 good CRs with $\text{RUWE}_{\text{DR3}} > 2$, 15 also showed secondary periods in the TESS light curves. Considering the weaker threshold of $\text{RUWE}_{\text{DR3}} > 1.4$, 18/21 such CRs showed secondary TESS periods.

Table 1 summarizes each of the above sources of information into a single bitwise column. We discuss possible connections between binarity and the CR phenomenon in Section 5.2.

4. CR EVOLUTION

4.1. Evolution over two year baseline

Figure 6 shows “before” and “after” views of 27 CRs for which TESS 120-second cadence observations were available at least two years apart. Such a baseline was available for 32 of the confirmed 50 CRs in our catalog; for plotting purposes we show the brightest 27. We have defined $\phi = 0$ for each sector to be the time of minimum light observed in that sector, rather than using a consistent phase definition across multiple sectors. This is because for most of the sources we do not know the period at the precision necessary to be able to accurately propagate an ephemeris over two years. The achievable period precision, σ_P , can be estimated as

$$\sigma_P = \frac{\sigma_\phi P}{N_{\text{baseline}}}, \quad (9)$$

for N_{baseline} the number of cycles in the observed baseline and σ_ϕ the phase precision with which any one feature (e.g. a dip, or the overall shape of the sinusoidal envelope) can be tracked. Assuming $\sigma_\phi \approx 0.02$ and a 20-day baseline over a single TESS sector yields $\sigma_P \approx 0.25_{-0.14}^{+0.38}$ minutes for the population shown in Figure 6; propagated forward 1,000 cycles yields a typical ephemeris uncertainty range of 2–11 hours. Measuring the period independently for each sector did not reveal evidence for significant ($> 3\sigma$) changes in period, implying a period stability of $\lesssim 0.1\%$ over two years.

A few objects in Figure 6 show the CR phenomenon in one sector, and only marginal signs or no sign of CR behavior in the other sector. In our subjective assessment,

⁴ For an explanation of the renormalized unit weight error (RUWE), see the GAIA DPAC technical note http://www.rssd.esa.int/doc_fetch.php?id=3757412.

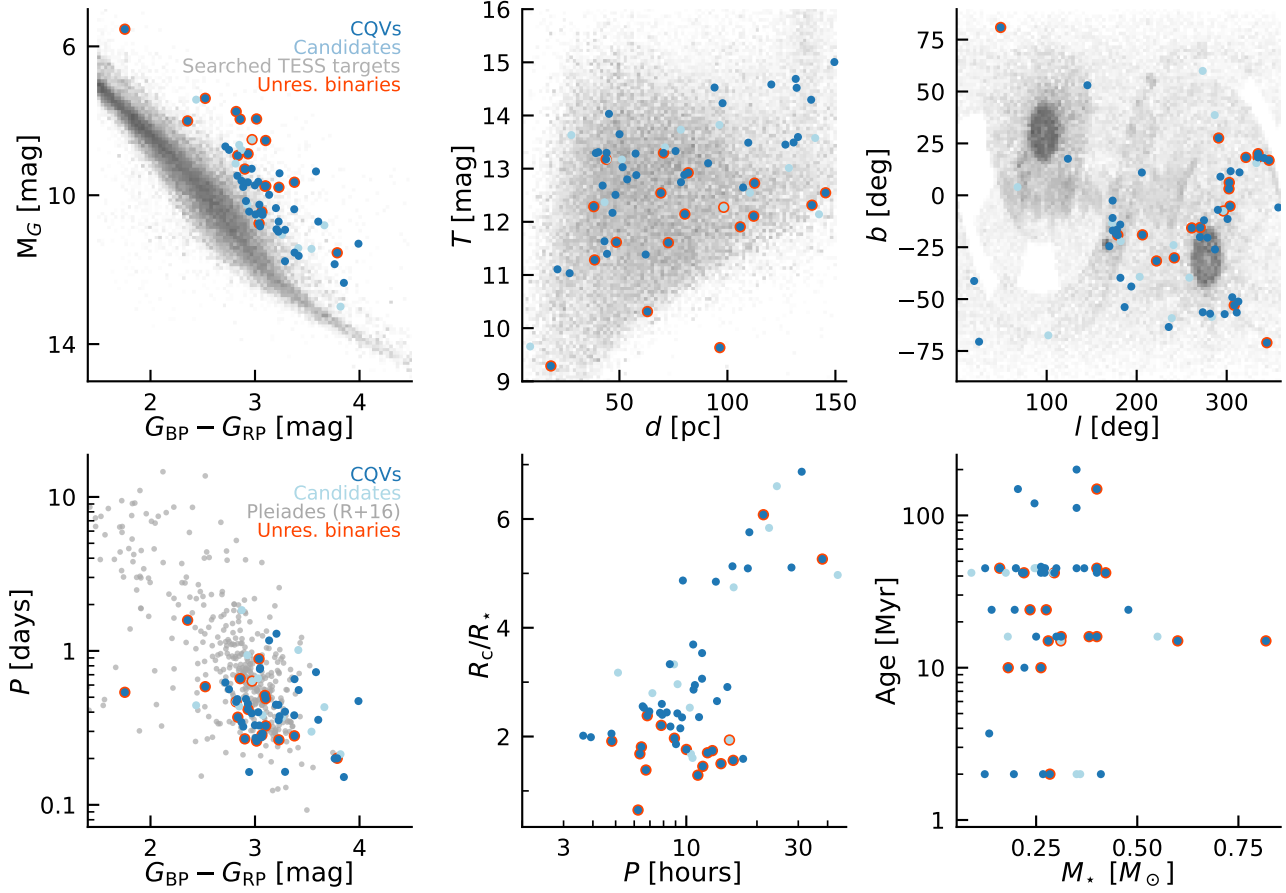


Figure 5. Properties of CRs identified by our search. CRs are mostly pre-main-sequence M dwarfs, younger than ≈ 150 Myr, with rotation periods faster than ≈ 1 day. The 50 bona fide CRs in Table 1 are the dark blue circles; 13 ambiguous CR candidates are light blue circles. Unresolved binaries (red circles) are objects for which the Gaia DR3 radial velocity scatter exceeded 20 km s^{-1} , or if $\text{Gaia RUWE}_{\text{DR3}} > 2$ and multiple photometric signals were present in the TESS light curve. The top panels show the 65,760 target stars with 120-second cadence TESS data as the shaded gray background; darker regions correspond to a larger relative number of searched stars. The lower-left panel compares the rotation–color distribution of CRs against the rotation periods of K and M dwarfs in the Pleiades from Rebull et al. (2016). The lower-middle panel plots the derived corotation radii $R_c = (GM/\Omega^2)^{1/3}$ in units of stellar radii against the measured CR periods, in units of hours. Ages in the final panel are known from cluster membership.

cases for which at least one sector would be flagged as “ambiguous” include TIC 368129164 (Sector 23 might be labeled an EB), TIC 177309964 (Sector 38 would be simply a rotating star), TIC 404144841 (Sector 38 looks like a rotating star), TIC 201898222 (Sector 3 looks like a rotating star), TIC 144486786 (Sector 32 might be an RS CVn), and TIC 38820496 (Sector 28 might be an RS CVn). TIC 193831684, assessed on a single-sector basis, would probably be labeled an eclipsing binary—in fact, Justesen & Albrecht (2021) already gave this source such a label. However, based on the shape evolution between Sectors 13 and 39, it is a CR. Based on the fraction of sources overall that “turned off”, the observed shape evolution implies that CRs have an on-off duty cycle of $\approx 75\%$. Correcting for the duty cycle might be important in population-level estimates of the intrinsic frequency of the CR phenomenon (e.g. Günther et al. 2022).

4.2. Evolution over consecutive sectors, & LP 12-502

A few of our complex rotators were near the TESS continuous viewing zones (Figure 5, top right). Out of this already small sample, LP 12-502 (TIC 402980664; $d=21 \text{ pc}$, $J=9.4$, $T=11.1$) stood out due to the quality and content of its data. We discuss another interesting source, TIC 300651846, in Appendix B. In this section, we describe the LP 12-502 observations and the possible implications.

4.2.1. LP 12-502 observations

Whenever LP 12-502 was located within a TESS sector, it was observed at 120-second cadence. Figure 7 shows all the available data, from Sectors 18, 19, 25, 26, 53, 58, and 59. Vertical offsets were applied to separate the data from different spacecraft orbit numbers; there are always two orbits per sector. We binned the light curve to 15-minute intervals to facilitate visual inspection. Points more than 2.5σ above

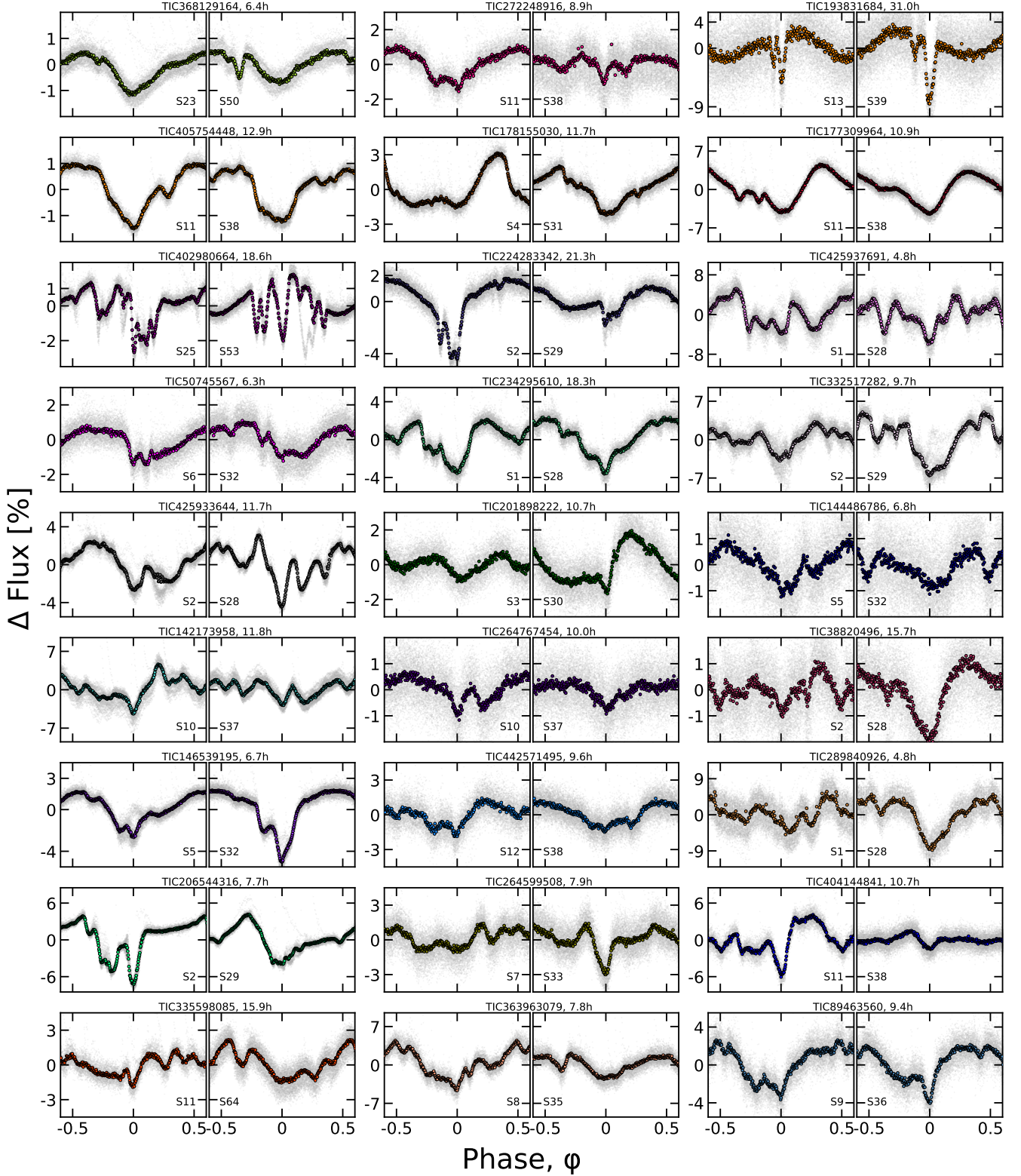


Figure 6. Evolution of CR light curves over two years. Out of the 50 CRs in Figure 4, 32 had 120-second cadence TESS data available for a baseline of at least two years; the 27 brightest are shown here due to space constraints. Each panel shows one sector of TESS data, and is phased to its deepest minimum in flux. Each panel's title shows the TIC identifier and period in hours. Text insets show the TESS sector numbers, which generally span two years, or at least 1,000 cycles. The vertical scale is fixed across sectors to clarify shape changes. Gray circles are raw 2-minute data; colored circles bin to 300 points per cycle.

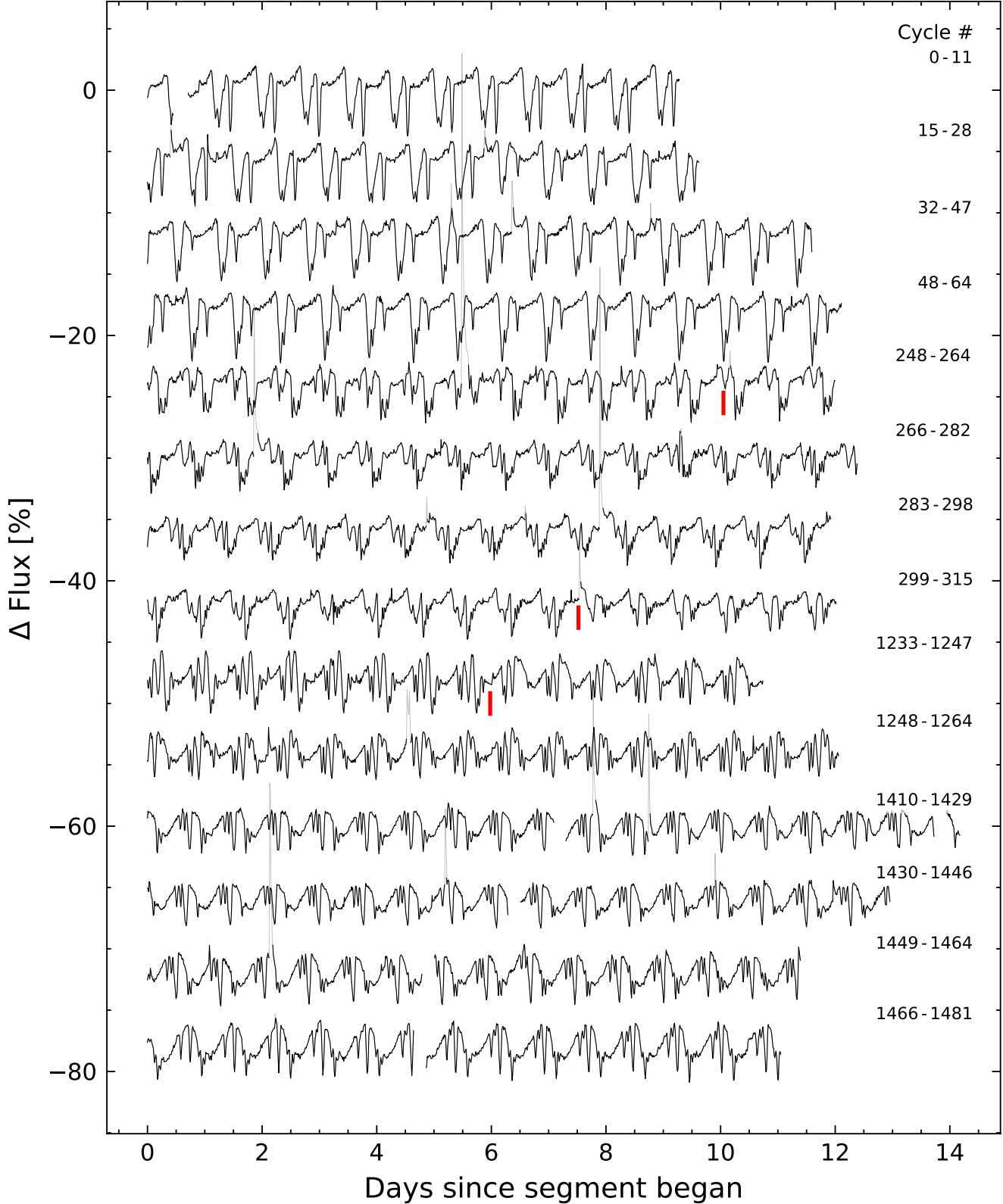


Figure 7. LP 12-502 (TIC 402980664) light curve, where each time segment represents one TESS orbit. Data were acquired in Sectors 18-19, 25-26, 53, and 57-58. Flares are drawn in gray. The light curve is binned to 15-minute intervals so that there are 96 points per day, and each point is connected by a line. Data gaps have nothing plotted. The red vertical lines highlight apparently instantaneous state changes in the shape of the dip pattern.

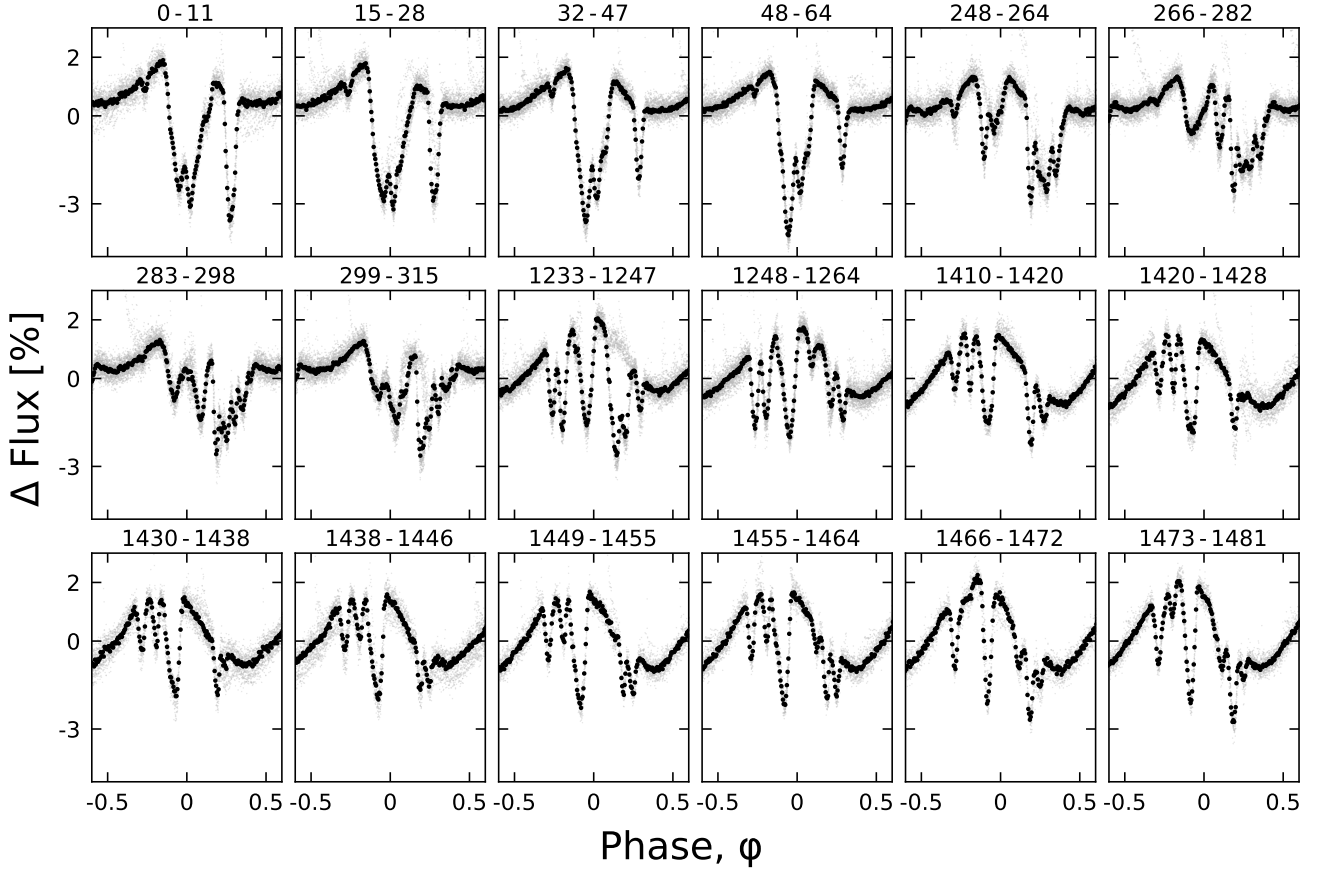


Figure 8. Evolution of LP 12-502 ($P=18.5611$ h) at fixed period and epoch over three years. Each panel shows one (averaged) TESS orbit; small text denotes relative cycle number. There are 200 binned black points per cycle. The TESS pointing law dictates the large time gaps between cycles 64–248, 315–1233, and 1264–1410; larger gaps tend to yield larger shape changes. The dips usually evolve over tens to hundreds of cycles. However cycles 1233–1264 show a dip that switched from a depth and duration of 3% and 3 hr to 0.3% and 1 hr over less than one cycle (cf. Figure 7).

the median are drawn in gray, to prevent outliers from seizing attention. Data gaps are not connected by lines (a common source of confusion in light curve visualization). Figure 8 shows the same data after phase-folding each TESS spacecraft orbit, assuming $P=18.5611$ hr and a fixed reference epoch of BTJD=1791.5367. Finally, Figure 9 shows “river plots” of the same data, split into similar intervals: the Sector 18–19 data, 25–26 data, 53 data, and 58–59 data. The river plots are subject to one additional processing step: we fitted and subtracted a maximum-likelihood two-harmonic sinusoid independently from the Sector 18–19 data, 25–26 data, and 53, 58, and 59 data in order to accentuate changes in the dip timing and structure.

The average period, determined by measuring the PDM peak period over each sector independently, was $\langle P \rangle = 18.5560$ hr. The range between the maximum and minimum sector-specific periods was measured to be about one minute. However, a period shift of ± 1 minute leads to large phase drifts over the entire timespan of observations. One minute is $\approx 1/1000^{\text{th}}$ of a period, and we have observed 1500 cycles. By folding with a fine grid of trial periods, we found that the

choice $P = 18.5611 \pm 0.0001$ causes more of the features in the LP 12-502 light curve to maintain constant phases over the entire dataset.

We now attempt to describe the complex morphology of the light curve and its evolution. For the first 64 cycles, the star shows four obvious local minima. We dub these dips {1, 2, 3, 4} at phases {−0.28, −0.08, 0, 0.25}, respectively. Dips 2 and 3 are part of the same “global” minimum, which otherwise resembles a long eclipse. Over cycles 0–64, the depth of dips 1 and 3 remain roughly fixed. Dip 4 decreases in depth by about 2%, and dip 2 increases in depth by about the same amount (see Figure 8). A subtle fifth dip may also be present at phase +0.08, at the end of the global minimum that includes dips 2 and 3.

There is then a 6-month (184-cycle) gap to Cycles 248–315, which show two highly structured dip complexes, plus a small leading dip. The leading dip has the same phase (relative to minimum light) as in cycles 0–64, and therefore seems likely to be due to the same structure. Along a similar line of logic, it seems plausible that the first “dip complex” during cycles 248–264 represents an evolution and reduction in

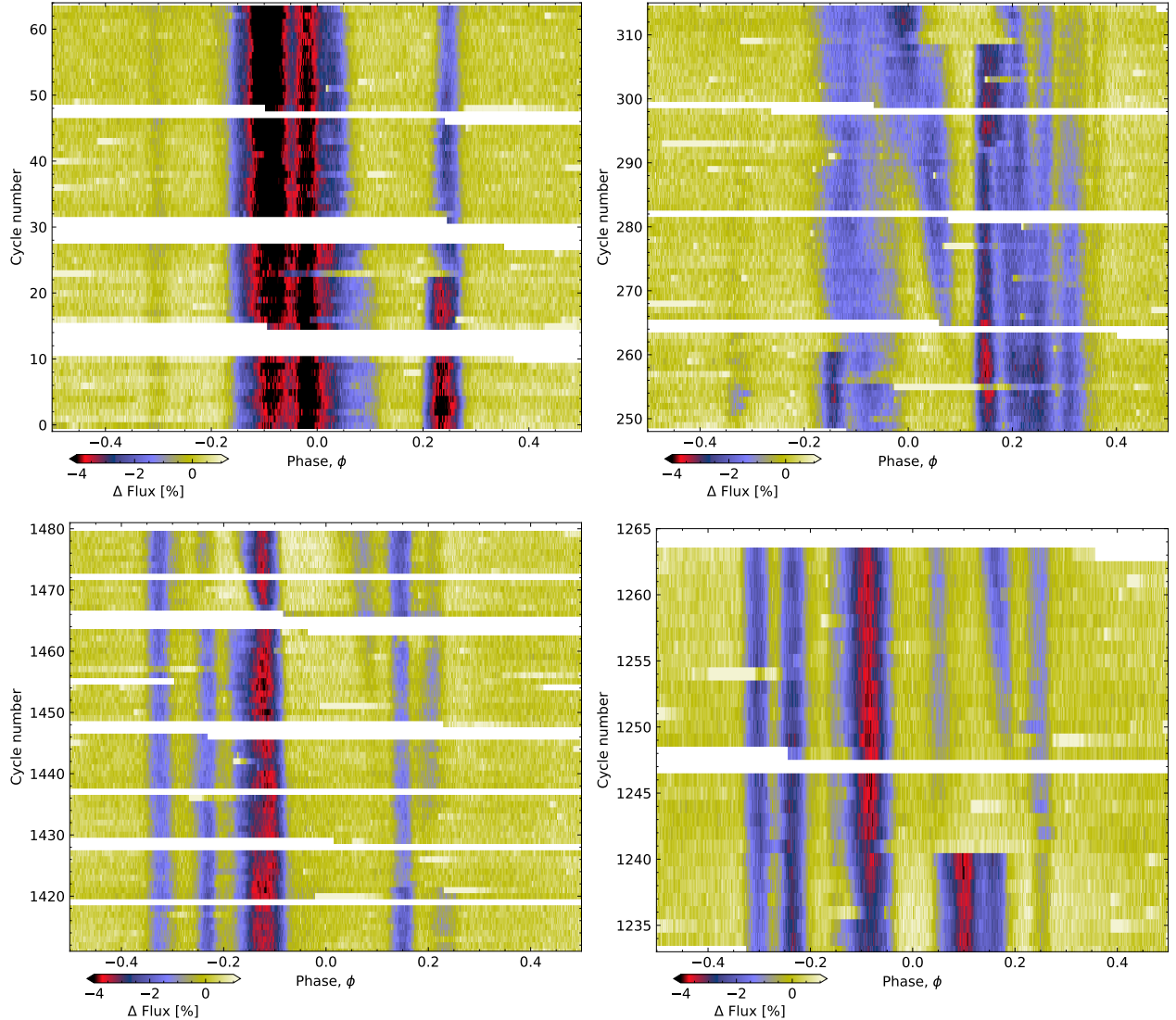


Figure 9. River plots of the LP 12-502 light curve, showing (clockwise from top-left) Sectors 18-19, 25-26, 53, and 58-59. A two-harmonic sinusoid has been subtracted to highlight the sharp dips. A fixed period and phase are adopted for all sectors; the dips across all observations are bounded by $\phi \in [-0.35, 0.35]$. In Sectors 25-26 (cycles 248-315), periods are visible at the fundamental period of 18.5611 hr, as well as at faster ($\phi \approx 0.07$) and slower ($\phi \approx 0.25-0.27$) relative periods based on the presence of blue dips with distinct slopes. Multiple simultaneous periods are also visible in Sector 53 (cycles 1234-1263) and Sectors 58-59 (cycles 1411-1479). White chunks denote missing data. The state changes noted in red in Figure 7 occur in cycles 261, 309, and 1241.

amplitude of dips 2 and 3 that were seen during cycles 0-64. During cycles 266-310, an additional local minimum develops between the two complexes; this feature is best visualized on the river plots (Figure 9), where it is seen to have a shorter period than the other dips (as described below).

The second dip complex during cycles 248-315 shows the most substructure. During e.g. cycles 283-298, this single complex shows six local minima. The first and deepest dip is sharp: it shows a flux excursion of 3.5% over about 22 minutes ($0.02 P$), which is the steepest slope exhibited anywhere in the LP 12-502 dataset. After the sharp dip, there is a roughly exponential return to the baseline flux spanning about a quarter of a period, punctuated by coherent local min-

ima and maxima that the river plot (Figure 9) reveals to have slightly longer periods than the sharp dip. The sharp leading dip remains roughly constant in amplitude until a sudden “state change” at BTJD 2030.7 (cycle 309) that occurred at the same time as a flare, and left the trailing dips seemingly unaffected. This apparent state change, and two others, are marked with red lines in Figure 7.

The behavior during Sectors 53–58 (cycles 1233-1481) is comparatively tame; the light curve shows only four to six dips per cycle. Some dips remain stable in depth and duration over this five-month interval. Other dips grow, like the one at $\phi = +0.06$ between cycles 1499 and 1481. Other dips, such as the one at $\phi = +0.12$ in cycles 1233-1264, disappear entirely.

The most dramatic state change occurs during cycle 1241, when a large dip switches from a depth of 3% and a duration of 3 hours to a depth of 0.3% and a duration of 1 hour.

4.2.2. Lessons from LP 12-502

STATE-CHANGES REVEAL DIP INDEPENDENCE—The state-changes seen in cycles 1233-1247 and 299-315 confirm that dips can disappear in less than one cycle. While such behavior was also noted by Stauffer et al. (2017), the data presented here show further that the dips can be *independent* and *additive*. For example, throughout cycles 1233-1264, there are three sharp dips between phases of 0 and 0.3 with different amplitudes but similar slopes. During the transition, the leading dip nearly disappeared while the other two dips hardly changed; compare the centermost two panels of Figure 8. Evidently, the material or process responsible for one dip can vary independently of the materials or processes responsible for other dips. The state changes during cycles 248-264 and 299-315 support the same conclusion, while also hinting that the *leading* dip of a complex is most prone to disappearing, leaving the trailing dips unchanged in its wake.

SLOW GROWTH; RAPID DEATH—LP 12-502 shows at least three instances in which dips switch off over less than one cycle; we did not see any such instances of dips switching on. Dip growth seems to happen more slowly. For instance, the dip at phase 0-0.1 between cycles 258-290 begins to become detectable during cycle 258, and growths in depth by about 2% over the next eight cycles. The evolution of this particular dip is most clear in the river plots. The evolution of the dip group at phases 0.1-0.3 during cycles 1410-1481 is another example of this slow mode of dip growth.

DIP DURATIONS—The shortest dip duration for any of the individual LP 12-502 dips seems to be $\approx 0.06 P \approx 1.08$ hr. This is very similar to the characteristic timescale of a transiting small body at the corotation radius,

$$T_{\text{dur}} \equiv R_{\star} P_{\text{rot}} / (\pi a) = 1.02 \pm 0.10 \text{ hr}, \quad (10)$$

where we have inserted the stellar radius and mass derived in Section 2.3. Thus, the shortest-duration dips could be produced by transits of bodies or distributions of material that are smaller than the star. The corotation radius corresponds to $a/R_{\star} \approx 5.8$, i.e., the transit of a body at the corotation radius has a duration about six times shorter than a feature on the stellar photosphere that is carried across the visible hemisphere by rotation. On the other hand, some dip durations are sufficiently long that an explanation involving transits would require structures that are larger than the star along the direction of orbital motion.

DIP PERIODS—Most of the LP 12-502 dips repeat with a period of $P = 18.5611 \pm 0.0001$ hr. However the river plots (Figure 9) reveal that a few dips have detectably distinct periods. For instance, in sectors 25-26, the dip that develops around cycle 262 has a period shorter than the mean period by $\approx 0.1\%$, and some of the trailing local minima in the main dip complex have periods slower than the mean period by $\approx 0.04\%$. In addition to the fundamental period, we were able

to identify at least four distinct periods shown by specific dips over the full Sectors 18-59 dataset: 18.5683, 18.5672, 18.5473, and 18.5145 hr, with a measurement uncertainty of ≈ 0.0002 hr. Possibly, the different periods belong to clumps of dust or prominences of gas at slightly different orbital distances surrounding the corotation radius.

5. DISCUSSION

5.1. Typical and extreme CRs

Referring back to Figure 5, which compares the properties of CRs with those of the search sample (top panels) and the Pleiades (Rebull et al. 2016), we see that the typical CR masses span 0.1 - $0.4 M_{\odot}$, and the typical ages span 2-150 Myr. This mass and age range includes both fully convective stars and stars with a combination of radiative cores and convective envelopes, with the dividing line at around $M_{\star} = 0.25 M_{\odot}$ (Baraffe & Chabrier 2018). We found no obvious differences in light curve morphology between CRs above and below the boundary of $0.25 M_{\odot}$. In terms of their rotation rates relative to the Pleiades, the CRs are among the more rapidly rotating half of M dwarfs.

The closest CR in our catalog is DG CVn (TIC 368129164; $d=18$ pc), a member of AB Dor. To our knowledge, this star had not previously been recognized as a CR. The three brightest CRs are DG CVn ($T=9.3$), TIC 405754448 ($T=9.6$), and TIC 167664935 ($T=10.3$). The shortest period, 3.64 hr, belongs to TIC 201789285. The longest period, 37.9 hr, belongs to TIC 405910546. If the latter source turns out to be an eclipsing binary, the longest-period CR in the catalog would be TIC 193831684 (31.0 hr). By definition, we required the periods to be below 48 hr.

The lowest mass ($\approx 0.12 M_{\odot}$) belongs to TIC 267953787. The catalog contains a few other stars with similar mass. We cannot rule out the possibility that CRs exist with even lower masses, given the small number of such low-mass stars in our target sample. Perhaps even brown dwarfs can be CRs, although it might be difficult to distinguish the type of variability we associate with CRs from the usual variability of brown dwarfs caused by clouds and latitudinal bands (e.g. Apai et al. 2021; Vos et al. 2022).

5.2. CRs and binarity

5.2.1. Binary statistics

In Section 3.4, we found that a significant fraction of the CRs show indications of unresolved binarity. Excess noise above the Gaia single-source astrometric model is common (16/50 high-quality CRs with $\text{RUWE}_{\text{DR3}} > 2$), as is the presence of multiple periods in the TESS light curves (22/50). Elevated astrometric noise is almost always accompanied by multiple detectable TESS periods (15/16 high-quality CRs). The latter observation corroborates the claim that most sources with $\text{RUWE}_{\text{DR3}} > 2$ are binaries with projected apparent separations below 1'', and projected physical separations $\lesssim 50$ AU.

One possible relation between binarity and CRs is that the presence of an intermediate-separation binary could cause

early disk dispersal, freeing the star to contract. The CR phenomenon seems to require rapid rotation; thus if binary systems tend to produce more rapidly rotating stars, we would expect a sample of CRs to have a larger binary fraction than the field. We do not see clear evidence for such an effect. The multiplicity rate of M dwarfs near the Sun is $26.8 \pm 1.4\%$ (Winters et al. 2019). Based on the same study, the peak of the separation distribution decreases from ≈ 49 AU for 0.30–0.60 M_{\odot} stars, to ≈ 11 AU for 0.15–0.30 M_{\odot} M dwarfs. The multiplicity fraction in our CR sample seems approximately consistent with this field fraction.

5.2.2. Do K dwarf CRs exist?

To date, the only stars reported to show the CR phenomenon are M dwarfs, with typical stellar masses $\lesssim 0.3 M_{\odot}$ (Stauffer et al. 2017; Günther et al. 2022). However the two most massive CRs in our sample, TIC 405754448 and TIC 405910546, were assigned masses of $\approx 0.82 M_{\odot}$ and $\approx 0.60 M_{\odot}$ respectively. The next-highest masses in our sample are $\approx 0.40 M_{\odot}$.

These stars’ locations in color–absolute magnitude diagrams and their probable membership in Lower Centaurus Crux both support the conclusion that they have relatively high masses. However in detail, both are subject to ambiguities in interpretation. The TIC 405910546 light curve has a unique shape, suggestive of an eclipsing binary. Independently, TIC 405910546 was one of only three CRs flagged with a Gaia DR3 radial velocity scatter exceeding 20 km s^{-1} . Combined, these factors suggest that TIC 405910546 could be a pre-main-sequence eclipsing binary; it should be studied further to clarify this classification.

For the other object, TIC 405754448, the evidence for binarity is stronger. The RUWE_{DR3} statistic is 6.8, and the raw light curves in Sectors 11, 37, and 38 show both the CR signal with period 12.9 hr and amplitude $\approx 1\%$ and an additional sinusoidal signal with a period ≈ 6.5 days and amplitude $\approx 0.3\%$, likely from a second star. If TIC 405754448 is a K+M binary, then the flux ratio between the primary and secondary would be expected to be $\approx 10:1$. Thus, if the K star were the source of the CR signal, its intrinsic variability amplitude would be $\approx 1\%$, while if the M star were responsible its intrinsic variability amplitude would be $\approx 10\%$.

In short, these two objects suggest that the CR phenomenon may extend up in mass to pre-main-sequence K dwarfs, but more data are needed to substantiate this claim.

5.2.3. An astrophysical CR false positive: TIC 435903839

We originally classified TIC 435903839, with $\text{RUWE}_{\text{DR3}}=17.7$, as an “ambiguous” CR with a 10.8 hr period, because this period minimized the dispersion in the phase-folded light curve. More careful inspection revealed an impostor: this source is a photometric blend of two ordinary rotating stars with $P_0=3.60$ hr, and $P_1=5.41$ hr, giving a beat period $(P_0^{-1}-P_1^{-1})^{-1}$ of 10.8 hr. This is a novel false positive scenario for CRs: two rapidly-rotating stars with near-integer ratios of rotation periods. The beat between the two rotation signals produces the apparent CR signal. Such

false positives can be excluded through careful accounting of all peaks in a periodogram. For instance, TIC 435903839 shows a peak at 16.27 hr, which is not an integer multiple of the dispersion-minimizing 10.82 hr period.

5.2.4. Multiple CRs in the same system: TIC 425937691 and TIC 142173958

TIC 142173958 and TIC 425937691 both show evidence for two separate CR signals in their TESS light curves. For TIC 142173958, the signals have periods of 11.76 hr and 12.84 hr. For TIC 425937691, the two periods are 4.82 hr and 3.22 hr, near the 3:2 commensurability. Given that both sources have two photometric signals and elevated RUWEs, each source is probably an unresolved binary consisting of two CRs.

Recent work has shown that the orbits of binaries closer than $\lesssim 700$ AU tend to be aligned with their planetary systems (e.g. Christian et al. 2022). If we assume that observing CR variability requires high inclinations relative to the line of sight, and that the inclinations in binaries are correlated, then we would expect the detection of one CR in a binary system to raise the probability that the other star is a CR. The limitations of the current catalog prevent further exploration of this issue, but it might be interesting for future study. Even if this scenario is correct, it would not provide an immediate explanation for the near-commensurability of the two periods of TIC 425937691 (the ratio is within 1% of 3:2).

5.3. Transience & special phases of CR dips

While CR periods appear to remain constant to within measurement precision over thousands of cycles, the light curve shapes evolve over typical timescales of 10 to 1,000 cycles (e.g. Figures 6 and 9). The CRs are therefore quasiperiodic, with a characteristic dip longevity of ≈ 100 cycles. While this observation is consistent with the analyses by Günther et al. (2022) and Popinchalk et al. (2023), it marks a qualitative departure from the “persistent” vs. “transient” flux dip distinction described by Stauffer et al. (2017), since all CR dips seem to be transient over timescales of more than 1,000 cycles (Figure 6).

One peculiarity of CR evolution however is that the dips do not explore all phase angles with equal weight. LP 12-502, and other CRs, have preferred phases lasting for at least two years. For LP 12-502, all of the dips happen over phases corresponding to only two thirds of the period (Figures 8 and 9). The remaining third seems to be “out of limits” for dips over the timespan of observations. This could be evidence that the stellar magnetic field is not azimuthally symmetric. Alternatively, the source of the material (e.g. a planetesimal swarm) might be distributed over an arc rather than occurring randomly around the entire orbit.

5.4. Dip asymmetries and dust geometries

The asymmetry of a dip around the time of minimum light might be caused by the variation in optical depth of the occulting material as a function of orbital phase angle. Sharp

leading edges with trailing exponential egresses, for instance, have been previously seen for transiting exocomets and disintegrating rocky bodies (e.g. Rappaport et al. 2012; Brogi et al. 2012; Vanderburg et al. 2015; Zieba et al. 2019).

Examining Figure 4, it is clear that CR dips can be asymmetric but it is not obvious whether there is a preference for sharper ingresses or sharper egresses. In some cases (e.g. TIC 425933644), the flux variations do not resemble isolated dips, making the meaning of “ingress” and “egress” unclear. In other cases, such as Sector 36 of TIC 89463560, there is a sharp drop with an exponential return to the baseline flux, resembling the signatures of exocomet (e.g. Rappaport et al. 2018; Zieba et al. 2019), or the outflowing exospheres of certain transiting planets (e.g. McCann et al. 2019; MacLeod & Oklopčić 2022).

5.5. Dust vs. gas

Both the dust clump and the gas prominence scenario invoke clumps of material at the corotation radius; the main property that we believe distinguishes the two ideas is the composition of the material.

5.5.1. What is a prominence?

The prominence idea is based on an analogy with quiescent prominences/filaments in the solar corona that last as long as a few weeks (see Vial & Engvold 2015). In the context of the Sun, a prominence is a clump of cold, partially ionized hydrogen viewed in emission against the dark backdrop of space. A filament is the same clump of plasma, but viewed in absorption against the solar disk. In an extrasolar context, spectroscopic detections of transient Balmer- and resonance-line absorption seen for stars such as AB Dor and Speedy Mic (e.g. Collier Cameron & Robinson 1989; Jeffries 1993; Dunstone et al. 2006; Leitzinger et al. 2016) have been interpreted as prominences that scatter a star’s chromospheric emission (see Collier Cameron & Robinson 1989). The short-term mechanical stability of such gas configurations is theoretically plausible for rapidly rotating stars (Ferreira 2000; Waugh & Jardine 2022). To our best knowledge, this class of spectroscopic observation also has no viable alternative explanations.

We performed a simple visual examination of the TESS light curves for five prominence-hosting systems studied by Jardine & Collier Cameron (2019)—AB Dor, Speedy Mic, LQ Lup, HK Aqr, and V374 Peg—and detected no CR behavior. Assuming that spectroscopically observable prominence systems do not turn off, this would imply that they are not always accompanied by photometric CR-like dips: a link between the spectroscopic prominences that may exist around rapidly rotating low-mass stars and the CR phenomenon has yet to be made.

5.5.2. What is the microphysical source of opacity?

CRs show broadband flux variations that can be 1–2× deeper in the blue than in the red (Onitsuka et al. 2017; Bouma et al. 2020; Günther et al. 2022; Koen 2023). Dust

can naturally explain this chromaticity, since it has a larger absorption cross-section in the blue than the red (e.g. Cardelli et al. 1989). Gas might also explain the observed chromaticities (Gray 1992). While bound-bound absorption can be excluded, since it provides opacity only at narrow resonant lines, the (neutral) hydrogen opacity due to bound-free absorption is “jagged” (see Gray 1992, Figure 8.5 and Eq. 8.8), such that at temperatures of $\approx 3,000$ K to $\approx 10,000$ K the opacity can be larger at blue wavelengths than at red wavelengths. Bound-free absorption of H $^{-}$ is often important at such temperatures, but this opacity source is stronger in the red than the blue, the opposite of what is required to produce deeper dips in the blue than in the red. Likewise, Thomson scattering is too gray to be the dominant opacity source.

An instructive point of comparison is the rapidly rotating magnetic B star, σ Ori E, which shows dips that are deeper in the blue than in the red (Hesser et al. 1977). Photometric and spectroscopic observations of this star have been understood in terms of a warped torus of corotating circumstellar material (Landstreet & Borra 1978; Nakajima 1985; Townsend et al. 2005). The circumstellar material is unlikely to be dust, which would sublimate quickly at the distance of the torus from the star.⁵ The opacity source for σ Ori E and its analogs is instead thought to be bound-free absorption by neutral hydrogen (Nakajima 1985), although to our best knowledge direct evidence for this conclusion has yet to be acquired. Separate and smaller-amplitude continuum flux brightenings in σ Ori E may also come from electrons scattering photospheric light toward the observer when the clouds are not transiting (Berry et al. 2022).

Given these complexities, it seems important for a future theoretical study to be conducted to determine to what degree the observed chromaticities in CRs match, or do not match, expectations from radiative transfer. This issue has a key ability to resolve the question of whether the CRs are explained by dust or by gas, which has bearing on whether the material producing the dips is coming from the star, or whether it is a byproduct of the protoplanetary disk.

5.5.3. The lifetime constraint

The observed lifetime of the CR phenomenon could provide another way to discern between the gas and dust clump scenarios. Based on the available statistics from e.g. Rebull et al. (2022) and references therein, it seems plausible that CR occurrence decreases with stellar age from $\approx 3\%$ at 10 Myr (Sco-Cen), to $\approx 1\%$ at 100 Myr (Pleiades), down to 0% by the ≈ 700 Myr age of Praesepe. This is odd in the context of the prominence scenario, because pre-main-sequence M dwarfs spin up over the first 100 Myr; prominences might therefore even be expected to be *more* common at 100 Myr than at 10 Myr, under the assumption that the production of

⁵ Zhan et al. (2019) explored the sublimation timescales for a canonical CR with $M_{\star} = 0.2 M_{\odot}$, $R_{\star} = 0.3 R_{\odot}$, and $T_{\text{eff}} = 3200$ K. They found that non-shielded, generic silicate dust mixture (Draine 1985) with a single size of $0.1 \mu\text{m}$ reached the ≈ 1500 K sublimation temperature at $\approx 3 R_{\star}$. This suggests that dust sublimation could be an important effect even for CRs.

prominences depends only on the stellar rotation rate. The dust clump scenario would hold a natural explanation: the lower occurrence of CRs around older stars would simply reflect a finite supply of dust. One possible complication however is that the magnetic field topology of rapidly rotating M dwarfs may depend on factors other than the rotation rate (e.g. the age), which might affect the production of prominences.

5.6. Planets or planetesimal swarms near corotation?

Close-in planets are common around M dwarfs; studies from Kepler have shown that early M dwarfs have ≈ 0.1 planets per star with sizes between $1\text{--}4 R_{\oplus}$ and orbital periods within 3 days (Dressing & Charbonneau 2015). The frequency of planets per star increases to ≈ 0.7 when considering periods as long as 10 days. Extrapolating to all small ($0.1\text{--}4 R_{\oplus}$) planets within 10 days, it is reasonable to expect nearly all M dwarfs to have at least one planet.

In the context of disk-driven planet migration, the stopping location for the innermost planet is set by the location of the protoplanetary disk's truncation radius (Izidoro & Raymond 2018). The truncation radius is traditionally calculated by equating the magnetic pressure from the stellar magnetosphere with the ram pressure of the inflowing gas. As it happens, the truncation radius is close to the corotation radius for low accretion rates (Hartmann et al. 2016; Li et al. 2022). These considerations invite us to imagine one or more planets migrating inward due to gas drag, and arriving at $\approx 5\text{--}10$ stellar radii before the disk is depleted.

With this picture in mind, it is tempting to attribute features of the CR light curves as transits of material ejected by planets or planetesimals. Young rocky bodies are expected to be hot, and they might expel either gas or dust. The Jupiter-Io system (e.g. Saur et al. 2004) is analogous, in that a small rocky body similarly feeds the construction of a plasma torus. We emphasize that while this type of configuration seems *a priori* plausible, no direct evidence currently supports it.

The main logical function of the planetesimals would be to serve as a source for the occulting gas or dust; they would not necessarily need to explain the observed phases of the observed dips. The azimuthal angle of the eventual entrainment would be entirely determined by the stellar magnetic field. In this scenario, the obscuring material would inspiral from one or more rocky bodies well beyond the corotation radius. The planetesimals themselves would not necessarily need to transit. However if they did, they would need to be $\lesssim 1 R_{\oplus}$ based on their non-detections in the TESS data. Possibly analogous systems include K2-22 (Sanchis-Ojeda et al. 2015) and KOI-2700 (Rappaport et al. 2014), though the obscuring material in the CRs would need to be observed much further from the emitting planet than for those two examples.

A more restrictive variant of the planetesimal scenario would be to posit that the obscuring material remains close to the launching body, similar to comets, or to the aforementioned K2-22 and KOI-2700 systems. If so, then the planetesimals would need to be at the corotation radius. One prediction would therefore be that certain orbital phases would

produce recurrent dips when observed over sufficiently long baselines, because the launching planetesimal would be massive enough to remain in orbit, while stochastically ejecting material. For most CRs (Figure 6), the data seem to be in tension with this expectation because the relative spacing between dips is almost never conserved. With that said, certain sources do seem to exhibit “special phases”, including LP 12-502 (TIC 402980664), DG CVn (TIC 368129164), TIC 193831684, and TIC 146539195. One possible explanation for this might be if obscuring material is remaining close to its launching body, or bodies. An alternative explanation could be that the stellar magnetic field configurations responsible for confining said material are stable over the existing two-year baseline.

5.7. From dippers to debris disks

About one in three young stars with infrared-detected inner dusty disks show quasiperiodic or stochastic dimming over timescales of roughly one day (e.g. Alencar et al. 2010). The dimming amplitudes can reach a few tenths of the stellar brightness, and dips with identical depths and phases rarely recur. These “dipper” stars are probably explained by occulting circumstellar dust in the inner disk (e.g. Cody et al. 2014; Ansdell et al. 2016; Robinson et al. 2021; Capistrant et al. 2022). While the phenomenon can persist beyond ≈ 10 Myr (Gaidos et al. 2019, 2022), in all such cases it seems to be associated with the presence of infrared excesses. Phenomenologically, dippers are different from CRs in that their dips are usually deeper, less periodic, and more variable in depth over timescales of only one or a few cycles. Dipper stars also tend to be younger, since they tend to be classical T Tauri stars with infrared excesses.

In identifying the two candidate CRs with outlying SEDs (TICs 193136669 and TIC 57830249; Section 3.3), we were prompted to reconsider our light curve-based labeling, and ultimately concluded that these sources are dippers. This episode suggests that there could be overlap between CRs and dippers. Taking TIC 57830249 as one example, the Sector 36 TESS data are suggestive of a CR, with relatively periodic, sharp dips with depths of a few percent. The Sector 10 data are completely different, varying in apparent flux by a factor of two, with no discernible periodicity at all. Perhaps this source becomes a “dipper” when an inflow of dust reaches the inner disk wall, and is otherwise a “CR” when the inner disk is starved of dust.

Although this outlier is intriguing, stars without infrared excesses typically have more stable optical light curves than those with infrared excesses. While some dippers may evolve into CRs after the disk is mostly gone, this would be generically expected based on the population statistics: young stars become older. There may be no other causal connection between the two evolutionary stages. With that said, a common mystery between the CRs and dippers is how exactly the *narrowness* of the dust-induced dimmings is produced. It is not unreasonable to imagine a similar mechanism operating for both types of object, tied perhaps to a shared magnetic topol-

ogy, or perhaps to a preference for dust to inspiral to the star in clumped structures.

5.8. Mass flux estimate

Assuming for the moment that the obscuring material is dust, we can estimate the mass of a transiting clump. First, we convert the transit depth into an effective cloud radius, R_{cloud} . For most CRs in Figure 4, this yields $\approx 2\text{-}20 R_{\oplus}$. A minimum constraint on the number density of dust particles is obtained by requiring the cloud to be optically thick. For cases like LP 12-502, this is reasonable because the transit duration of the shortest dips implies $R_{\text{cloud}} \ll R_{\star}$. Carrying out the relevant calculation assuming the dust grains are $1 \mu\text{m}$ in size, Sanderson et al. (2023) reported minimum cloud masses of order 10^{12} kg (their Eq. 23), which scale linearly with both the optical depth and dust grain radius. This is comparable to a small asteroid; the asteroid belt itself has a mass of order $\approx 10^{21}$ kg (Park et al. 2019). A similar calculation that assumed occulting clumps of hydrogen, rather than dust, derived gas prominence masses of at least 10^{14} kg (Collier Cameron et al. 1990), about $100\times$ larger than the lower limit on the dust mass.

If the disappearance of a dip represents the permanent loss of the obscuring material – for example, if it is the result of a dust clump being accreted or ejected – then we can also estimate the rate at which mass is flowing through the structures that lead to dips. For instance, LP 12-502 showed three “state-switch” events over the six months of available TESS observations, during cycles 261, 309, and 1241 (Figure 9). The other source for which we performed a comparable analysis, TIC 300651846 (Appendix B), showed two state-switches over 11 months. In all such cases, at least one dip turned off. For purposes of estimation, we will take LP 12-502 as our prototype. Assuming the occulting material is dust, the corresponding $\dot{M} \equiv M \cdot dN/dt$ time-averaged over six months is $\approx 3 \times 10^{-18} M_{\odot} \text{ yr}^{-1} \approx 1 \times 10^{-12} M_{\oplus} \text{ yr}^{-1}$. Considered cumulatively over the $\approx 10^8$ years for which the CR phenomenon is observed, this yields a cumulative moved dust mass of $10^{-4} M_{\oplus}$, of order the Solar System’s asteroid belt. If the occulting material is gas, the masses involved would be of order 100 times larger. For cases in which we observe the growth of dips, such as the Sector 29 data for TIC 224283342, or Sector 5 of TIC 294328885, the dip depths typically increase by of order a few percent over ten to twenty days. This growth rate yields a mass flux one order of magnitude larger than the earlier estimate.

5.9. Strengthening the magnetic B star connection

Stauffer et al. (2017) previously noted a possible connection between the CRs and rapidly rotating magnetic B stars such as σ Ori E, which can have circumstellar gas clouds trapped in corotation (Townsend et al. 2005). The σ Ori class is distinct from Be-star decretion disks, which do not have any obvious connection to the stellar magnetic field (Rivinius et al. 2013).

An argument against the connection between CRs and the σ Ori E analogs is that the light curve of σ Ori E is simpler

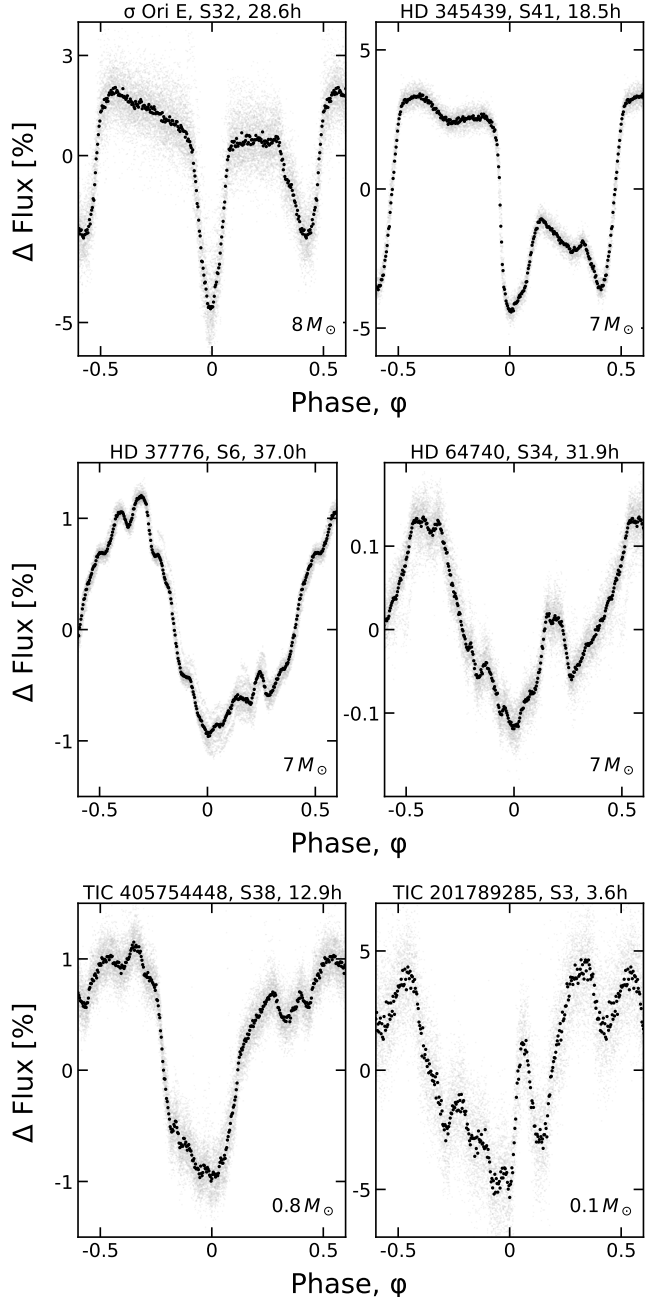


Figure 10. The magnetic B star connection. σ Ori E and HD 345439 (top row) are magnetic B stars with predominantly dipolar magnetic fields known to host circumstellar plasma tori. HD 37776 and HD 64740 (middle row) are analogous magnetic B stars with field topologies dominated by high order multipoles. The bottom row compares the latter systems against the “best-matching” CR light curves, selected by eye from Figure 4. CRs have light curves that are visually similar to the topologically complex magnetic B stars. Stellar masses rounded to one significant figure are given in the lower right of each panel; the star, TESS sector, and period are listed in each subtitle.

than those in Figure 4, with only two broad local minima, and one “hump” (Figure 10; see also Jayaraman et al. 2022). Within the model proposed by Townsend et al., the simplicity of the light curve is the result of a simple dipolar magnetic field, which is typical of magnetic B stars (Aurière et al. 2007; Donati & Landstreet 2009). The magnetic axis needs to be tilted relative to the stellar spin axis in order to match the qualitative behavior of both the broadband light curves, and the line-profile variations seen in hydrogen, helium, and carbon (Oksala et al. 2012).

Two interesting and possibly telling exceptions to the rule that magnetic B stars have simple light curves are HD 37776 and HD 64740. Both stars are known from spectropolarimetry to have field geometries dominated by high order multipoles (Kochukhov et al. 2011). And, recent TESS light curves of these two B stars appear surprisingly similar to the CR light curves (Mikulášek et al. 2020). The middle row of Figure 10 shows the phased TESS light curves for these two stars, with by-eye best-matching CRs shown underneath for comparison. The number of dips per cycle, the shapes of the dips, and the dip depths relative to the sinusoidal envelope are all similar. This connection suggests that the highly structured light curves of both the M dwarfs and the B stars are associated with (and perhaps caused by) strong non-dipolar magnetic fields. Non-dipolar fields for M dwarfs are plausible, given that Zeeman Doppler Imaging has revealed non-axisymmetric magnetic field patterns for the few M dwarfs for which this technique is technically feasible (see Kochukhov 2021, and references therein).

The physical similarity between the B stars and the M dwarfs presumably has its origin in the existence of a “centrifugal magnetosphere” (see Petit et al. 2013). In other words, both classes of objects probably satisfy the condition $R_m > R_c$, for R_m the magnetosphere radius (sometimes called the Alfvén radius). Provided that charged particles are confined to move along magnetic field lines, stable points that balance the centrifugal force and gravity can then exist at the corotation radius (e.g. Townsend & Owocki 2005). In the converse “dynamical” case, when $R_m < R_c$, material interior to the magnetospheric radius returns to the stellar surface over the free-fall timescale. A simple estimate assuming a dipole field with $B_0 \approx 1\text{ kG}$ at the star’s surface, a local plasma number density $n \approx 10^9\text{ cm}^{-3}$, and a plasma temperature 10^6 K gives magnetospheric radii of order a few times the corotation radii, R_c . This suggests that the existence of a centrifugal magnetosphere is plausible for young, rapidly rotating M dwarfs.

6. CONCLUSIONS

In this work, we searched 120-second cadence TESS data collected from 2018 July to 2022 September for complex rotators (CRs). The target stars were 65,760 K and M dwarfs within 150 pc. The selection function was $>80\%$ complete within 30 pc, and $<10\%$ complete at distances exceeding 100 pc.

In our target sample, we found 50 objects that showed complex quasiperiodic behavior over at least one TESS sec-

tor. These 50 bona fide CRs are listed in Table 1. This table also includes 13 ambiguous CRs, whose designation is less certain, and 3 impostors. We inferred ages for all but two of the 66 objects based on memberships in young stellar associations; we also derived temperatures and radii using SED fitting, and inferred stellar masses by interpolating against stellar evolutionary models. We caution that our sample is far from being volume-limited and is not even magnitude-limited: the TESS 120-second stellar sample had a heterogeneous selection function which may have been biased in favor of young stars over field stars. Previous work however has shown that $\approx 1\text{-}3\%$ of M dwarfs younger than $\approx 100\text{ Myr}$ show the CR phenomenon (Rebull et al. 2016; Günther et al. 2022).

Analyzing the TESS light curves and stellar properties of our CRs, we draw the following conclusions.

1. The sharpest CR dips have durations of $\approx 0.05 P$ and depths of $\approx 1\text{-}3\%$ (Figures 4 and 6). Explaining dips this sharp requires material extrinsic to the stellar surface (see Section 1).
2. The shortest CR dips, also with durations of $\approx 0.05 P$, match the expected transit duration of a small body at the corotation radius, $T_{\text{dur}} \equiv R_\star P_{\text{rot}} / (\pi a)$ (see Section 4.2.2). Such dips may therefore be produced by transits of bodies or distributions of optically-thick material that are smaller than the star.
3. Most CR dips have durations a few times longer than T_{dur} (Figure 4). The dips are often superposed on a quasi-sinusoidal signal that presumably comes from starspots and faculae that produce inhomogeneities in the longitudinal flux distribution across the stellar surface. The only viable explanation currently known for the sharp dips being superposed on the quasi-sinusoidal signals is that concentrations (“clumps”) of circumstellar material are corotating with the star. Assuming that the longer dips have the same physical origin as the shortest dips, the transiting material must therefore also be capable of having effective sizes comparable to the star.
4. The mean periods of CRs remain fixed to within a relative precision $\lesssim 0.1\%$ over the two-year ($\approx 1,000$ cycle) baseline of available observations. The light curve shapes always evolve over this timescale (Figure 6).
5. The dips in CR light curves can have slightly different periods. LP 12-502, for instance, showed dips with four distinct periods within $\pm 0.3\%$ of its fundamental period, sometimes simultaneously, and each lasting for up to 50 cycles (Figure 9).
6. The CR peaks and dips evolve over timescales that are both secular (≈ 100 cycles) and impulsive (< 1 cycle). Dip growth seems to happen over durations of at least ten cycles, and slow dip decay can also occur. “State-switches” correspond to dips collapsing instantaneously, and are almost always linked with observed optical flares. Such

- switches are suggestive of magnetic reconnection opening the “magnetic cage” that traps the dust.
7. The on-off duty cycle for CRs seems to be $\approx 75\%$, based on the fraction of bona fide CRs that either turned on or turned off during TESS re-observations, two years after the initial observation (Figure 6).
 8. The CR phenomenon persists for $\gtrsim 150$ Myr, based on the existence of multiple CRs in AB Dor, the Pleiades, and Psc-Eri (Section 2.3). It may even extend to 200 Myr, based on the one CR we found in the Carina Near moving group (TIC 294328887; ≈ 200 Myr). However the lack of detected CRs in the Hyades and Praesepe suggests that the lifetime of the phenomenon is limited to the first few hundred million years.
 9. Most CRs are M dwarfs with masses $0.1\text{-}0.5 M_{\odot}$. Two sources, TIC 405754448 and TIC 405910546, have masses that appear to exceed the M dwarf limit. However both are potentially binaries, and this may confuse our ability to accurately identify the source of the CR signal (Section 5.2.2). We encourage additional scrutiny of these objects in future work.
 10. The closest CRs to the Sun are at distances of 15-20 pc, and the brightest have $V \approx 12$ ($J \approx 7.5$). We have found most of them in this work, since our CR sample was $\gtrsim 80\%$ complete within 30 pc. The lack of CRs in the volume-complete < 15 pc sample of $0.1\text{-}0.3 M_{\odot}$ stars analyzed by Winters et al. (2021) is consistent with this estimate. Expanding our analysis of the TESS data to the full frame images would yield a truly volume-limited selection function, and would expand the CR census by about a factor of two within 50 pc, and by a factor of ten within 100 pc.
 11. Surprising analogs to the CRs exist in two magnetic B stars with multipolar field topologies. Since most magnetic B stars have dipolar magnetic fields, this suggests that the CR dips and warps are similarly being sculpted by the stellar magnetic fields, and that the magnetic fields themselves are potentially also multipolar.
 12. The rate of dip evolution can be used to place a model-dependent lower bound on how much material is either being accreted or ejected during the state changes (Section 5.8). Order of magnitude estimates require at least an asteroid belt’s worth of dust ($10^{-4} M_{\oplus}$) over 10^8 years, or at least $\approx 10^{-2} M_{\oplus}$ if the occulting material is gas.

While many questions remain, two in particular will be important for clarifying what these objects might teach us in a broader astrophysical context: 1) Is the eclipsing material responsible for the phenomenon gas or dust? 2) What sets the characteristic clumping size for the circumstellar material?

The distinction between gas or dust is important because it will clarify whether the CR phenomenon is intrinsic, so that material comes from the star, or extrinsic, so that it is

sourced through some generic evolutionary phase of debris disks. This knowledge would in turn propagate to our understanding of whether the phenomenon is primarily teaching us about dust production and processing in gas-poor disks, or whether it is teaching us about the ability of cold gas to remain stable in hot stellar coronae for long durations. Observationally, acquisition of medium- or high-resolution time-series spectra holds a good chance at resolving the gas vs. dust question. Given our observed $\approx 75\%$ on-off duty cycles, such data must be acquired simultaneously with photometric time-series observations (e.g. during TESS re-observation) in order for detections and non-detections to be interpretable.

In both the gas and dust scenarios, CRs are preferentially viewed edge-on. This implies that after correcting for the line-of-sight inclination, roughly one third of low mass stars (those that rotate rapidly enough; Günther et al. 2022) could trap circumstellar material in the same way. It also suggests that CRs may preferentially show transiting planets at larger distances than the corotating material, though this conclusion would be dependent on whether the magnetic and stellar spin axes tend to be aligned. Given these points, observational follow-up work should include searching for outer transiting planets, and measuring equatorial velocities in order to test whether the stellar inclination angles are indeed preferentially edge-on. Any source of empirical information on the stellar magnetic field, whether from the Zeeman effect (e.g. Kochukhov 2021) or perhaps radio emission (e.g. Hallinan et al. 2015), could also help clarify the strength of the magnetospheres for these objects.

On the theoretical front, building a physical understanding what sets the characteristic size scale of the clumping material would help clarify why the light curves have the bizarre shapes that are observed. The relevant puzzles in plasma physics and radiative transfer could perhaps be connected to our understanding of the close-in rocky planets that are expected to be present around most of these stars.

ACKNOWLEDGMENTS

LGB is grateful for support from the Heising-Simons 51 Pegasi b Fellowship, and for helpful conversations with G. Laughlin, A. Mann, and J. Spake. This paper relied on data collected by the TESS mission, which are available from the Mikulski Archive for Space Telescopes (MAST). The specific 120-second cadence observations can be accessed via DOI [10.17909/t9-nmc8-f686](https://doi.org/10.17909/t9-nmc8-f686). Funding for the TESS mission is provided by NASA’s Science Mission Directorate. TIC 402980664 in particular was observed at 120-second cadence thanks to the TESS Guest Investigator programs G022252 (PI: J. Schlieder; Sectors 18, 19, 25, 26) and G04168 (PI: R. Jayaraman; Sector 53). LGB is also grateful for the assistance of S. Yee, L. Weiss, H. Isaacson, and A. Howard in acquiring and analyzing the HIRES spectra.

LGB conceived the project and performed the dip-counting search, light curve classification, cluster membership, SED,

variability, and secondary-period analyses. RJ and SR performed the Fourier-based analysis and contributed to light curve classification. LR cross-examined the light curve classification, and contributed an independent SED analysis. AD identified the magnetic B star connection. LAH contributed to project design and to the interpretation of the light curves. JNW and SR significantly improved the clarity of the manuscript. GÁB acquired and maintained the servers used to run the dip-finding pipeline. All authors assisted in manuscript revision.

Software: astrobase (Bhatti et al. 2021), astropy (Astropy Collaboration et al. 2013, 2018, 2022),

lightkurve (Lightkurve Collaboration et al. 2018), numpy (Harris et al. 2020), pyGAM (Servén & Brummitt 2018), scipy (Virtanen et al. 2020), TESS-point (Burke et al. 2020), wotan (Hippke et al. 2019).

Facilities: Astrometry: Gaia (Gaia Collaboration et al. 2018, 2022). Imaging: Second Generation Digitized Sky Survey. Spectroscopy: Keck:I (HIRES; Vogt et al. 1994). Photometry: TESS (Ricker et al. 2015), Broadband photometry: 2MASS (Skrutskie et al. 2006), APASS (Henden et al. 2016), Gaia (Gaia Collaboration et al. 2018, 2022), SDSS (York et al. 2000), WISE (Wright et al. 2010).

REFERENCES

- Alencar, S. H. P., Teixeira, P. S., Guimarães, M. M., et al. 2010, *A&A*, 519, A88
- Allard, F., Homeier, D., & Freytag, B. 2012, *Philosophical Transactions of the Royal Society A: Mathematical, Physical and Engineering Sciences*, 370, 2765
- Ansdell, M., Gaidos, E., Rappaport, S. A., et al. 2016, *ApJ*, 816, 69
- Apai, D., Nardiello, D., & Bedin, L. R. 2021, *ApJ*, 906, 64
- Asplund, M., Grevesse, N., Sauval, A. J., & Scott, P. 2009, *ARA&A*, 47, 481
- Astropy Collaboration, Robitaille, T. P., Tollerud, E. J., et al. 2013, *A&A*, 558, A33
- Astropy Collaboration, Price-Whelan, A. M., Sipőcz, B. M., et al. 2018, *AJ*, 156, 123
- Astropy Collaboration, Price-Whelan, A. M., Lim, P. L., et al. 2022, *ApJ*, 935, 167
- Aurière, M., Wade, G. A., Silvester, J., et al. 2007, *A&A*, 475, 1053
- Bailer-Jones, C. A. L., Rybizki, J., Fouesneau, M., Demleitner, M., & Andrae, R. 2021, *AJ*, 161, 147
- Baraffe, I., & Chabrier, G. 2018, *A&A*, 619, A177
- Barber, R. J., Tennyson, J., Harris, G. J., & Tolchenov, R. N. 2006, *MNRAS*, 368, 1087
- Basri, G. 2021, An Introduction to Stellar Magnetic Activity
- Bell, C. P. M., Mamajek, E. E., & Naylor, T. 2015, *MNRAS*, 454, 593
- Berry, I. D., Owocki, S. P., Shultz, M. E., & ud-Doula, A. 2022, *MNRAS*, 511, 4815
- Bhatti, W., Bouma, L., Joshua, et al. 2021, waqasbhatti/astrobase: astrobase v0.5.3, Zenodo
- Bodman, E. H. L., Quillen, A. C., Ansdell, M., et al. 2017, *MNRAS*, 470, 202
- Bouma, L. G., Winn, J. N., Ricker, G. R., et al. 2020, *AJ*, 160, 86
- Bouma, L. G., Curtis, J. L., Masuda, K., et al. 2022, *AJ*, 163, 121
- Bressan, A., Marigo, P., Girardi, L., et al. 2012, *MNRAS*, 427, 127
- Briceño, C., Calvet, N., Hernández, J., et al. 2019, *AJ*, 157, 85
- Brogi, M., Keller, C. U., de Juan Ovelar, M., et al. 2012, *A&A*, 545, L5
- Burke, C. J., Levine, A., Fausnaugh, M., et al. 2020, TESS-Point: High precision TESS pointing tool, Astrophysics Source Code Library, record ascl:2003.001
- Cantat-Gaudin, T., & Anders, F. 2020, *A&A*, 633, A99
- Capistrant, B. K., Soares-Furtado, M., Vanderburg, A., et al. 2022, *ApJS*, 263, 14
- Cardelli, J. A., Clayton, G. C., & Mathis, J. S. 1989, *ApJ*, 345, 245
- Chen, Y., Girardi, L., Bressan, A., et al. 2014, *MNRAS*, 444, 2525
- Christian, S., Vanderburg, A., Becker, J., et al. 2022, *AJ*, 163, 207
- Cody, A. M., Stauffer, J., Baglin, A., et al. 2014, *AJ*, 147, 82
- Collier Cameron, A. 1999, in Astronomical Society of the Pacific Conference Series, Vol. 158, Solar and Stellar Activity: Similarities and Differences, ed. C. J. Butler & J. G. Doyle, 146
- Collier Cameron, A., Duncan, D. K., Ehrenfreund, P., et al. 1990, *MNRAS*, 247, 415
- Collier Cameron, A., & Robinson, R. D. 1989, *MNRAS*, 238, 657
- Curtis, J. L., Agüeros, M. A., Mamajek, E. E., Wright, J. T., & Cummings, J. D. 2019, *AJ*, 158, 77
- Dahm, S. E. 2015, *ApJ*, 813, 108
- David, T. J., & Hillenbrand, L. A. 2015, *ApJ*, 804, 146
- Donati, J. F., & Landstreet, J. D. 2009, *ARA&A*, 47, 333
- Draine, B. T. 1985, *ApJS*, 57, 587
- Dressing, C. D., & Charbonneau, D. 2015, *ApJ*, 807, 45
- Dunstone, N. J., Barnes, J. R., Collier Cameron, A., & Jardine, M. 2006, *MNRAS*, 365, 530
- Fausnaugh, M., Morgan, E., Vanderspek, R., et al. 2021, *PASP*, 133, 095002
- Feiden, G. A. 2016, *A&A*, 593, A99
- Ferreira, J. M. 2000, *MNRAS*, 316, 647
- Gagné, J., Mamajek, E. E., Malo, L., et al. 2018, *ApJ*, 856, 23
- Gaia Collaboration, Brown, A. G. A., Vallenari, A., et al. 2018, *A&A*, 616, A1
- Gaia Collaboration, Smart, R. L., Sarro, L. M., et al. 2021, *A&A*, 649, A6

- Gaia Collaboration, Vallenari, A., Brown, A. G. A., et al. 2022, arXiv e-prints, arXiv:2208.00211
- Gaidos, E., Jacobs, T., LaCourse, D., et al. 2019, *MNRAS*, 488, 4465
- Gaidos, E., Mann, A. W., Rojas-Ayala, B., et al. 2022, *MNRAS*, 514, 1386
- Gilbert, E. A., Barclay, T., Quintana, E. V., et al. 2022, *AJ*, 163, 147
- Gray, D. F. 1992, The observation and analysis of stellar photospheres., Vol. 20
- Gully-Santiago, M. A., Herczeg, G. J., Czekala, I., et al. 2017, *ApJ*, 836, 200
- Günther, M. N., Berardo, D. A., Ducrot, E., et al. 2022, *AJ*, 163, 144
- Hallinan, G., Littlefair, S. P., Cotter, G., et al. 2015, *Nature*, 523, 568
- Harris, C. R., Millman, K. J., van der Walt, S. J., et al. 2020, *Nature*, 585, 357
- Hartmann, L., Herczeg, G., & Calvet, N. 2016, *ARA&A*, 54, 135
- Henden, A. A., Templeton, M., Terrell, D., et al. 2016, VizieR Online Data Catalog, II/336
- Hesser, J. E., Ugarte, P. P., & Moreno, H. 1977, *ApJL*, 216, L31
- Hippke, M., David, T. J., Mulders, G. D., & Heller, R. 2019, arXiv:1906.00966 [astro-ph], arXiv: 1906.00966
- Hippke, M., David, T. J., Mulders, G. D., & Heller, R. 2019, *AJ*, 158, 143
- Howard, A. W., Johnson, J. A., Marcy, G. W., et al. 2010, *ApJ*, 721, 1467
- Howell, S. B., Sobeck, C., Haas, M., et al. 2014, *PASP*, 126, 398
- Izidoro, A., & Raymond, S. N. 2018, in *Handbook of Exoplanets*, ed. H. J. Deeg & J. A. Belmonte, 142
- Jardine, M., & Collier Cameron, A. 2019, *MNRAS*, 482, 2853
- Jayaraman, R., Hubrig, S., Holdsworth, D. L., et al. 2022, *ApJL*, 924, L10
- Jeffries, R. D. 1993, *MNRAS*, 262, 369
- Jenkins, J. M., Twicken, J. D., McCauliff, S., et al. 2016, in *Society of Photo-Optical Instrumentation Engineers (SPIE) Conference Series*, Vol. 9913, Software and Cyberinfrastructure for Astronomy IV, ed. G. Chiozzi & J. C. Guzman, 99133E
- Johns-Krull, C. M., Prato, L., McLane, J. N., et al. 2016, *ApJ*, 830, 15
- Justesen, A. B., & Albrecht, S. 2021, *ApJ*, 912, 123
- Kenyon, S. J., & Hartmann, L. 1995, *ApJS*, 101, 117
- Kerr, R. M. P., Rizzuto, A. C., Kraus, A. L., & Offner, S. S. R. 2021, *ApJ*, 917, 23
- Kochukhov, O. 2021, *A&A Rv*, 29, 1
- Kochukhov, O., Lundin, A., Romanyuk, I., & Kudryavtsev, D. 2011, *ApJ*, 726, 24
- Koen, C. 2021, *MNRAS*, 500, 1366
- . 2023, *MNRAS*, 518, 2921
- Lamb, F. K., Pethick, C. J., & Pines, D. 1973, *ApJ*, 184, 271
- Landstreet, J. D., & Borra, E. F. 1978, *ApJL*, 224, L5
- Leitzinger, M., Odert, P., Zaqrashvili, T. V., et al. 2016, *MNRAS*, 463, 965
- Li, R., Chen, Y.-X., & Lin, D. N. C. 2022, *MNRAS*, 510, 5246
- Lightkurve Collaboration, Cardoso, J. V. d. M., Hedges, C., et al. 2018, Lightkurve: Kepler and TESS time series analysis in Python, Astrophysics Source Code Library, record ascl:1812.013
- Long, M., Romanova, M. M., & Lovelace, R. V. E. 2005, *ApJ*, 634, 1214
- MacLeod, M., & Oklopčić, A. 2022, *ApJ*, 926, 226
- McCann, J., Murray-Clay, R. A., Kratter, K., & Krumholz, M. R. 2019, *ApJ*, 873, 89
- Mikulášek, Z., Krčíčka, J., Shultz, M. E., et al. 2020, in *Stellar Magnetism: A Workshop in Honour of the Career and Contributions of John D. Landstreet*, ed. G. Wade, E. Alecian, D. Bohlender, & A. Sigut, Vol. 11, 46
- Murphy, S. J., Lawson, W. A., & Bessell, M. S. 2013, *MNRAS*, 435, 1325
- Nakajima, R. 1985, *Ap&SS*, 116, 285
- Oksala, M. E., Wade, G. A., Townsend, R. H. D., et al. 2012, *MNRAS*, 419, 959
- Onitsuka, M., Fukui, A., Narita, N., et al. 2017, *PASJ*, 69, L2
- Paegert, M., Stassun, K. G., Collins, K. A., et al. 2021, arXiv e-prints, arXiv:2108.04778
- Palumbo, E. K., Montet, B. T., Feinstein, A. D., et al. 2022, *ApJ*, 925, 75
- Park, R. S., Vaughan, A. T., Konopliv, A. S., et al. 2019, *Icarus*, 319, 812
- Pecaut, M. J., & Mamajek, E. E. 2016, *MNRAS*, 461, 794
- Penoyre, Z., Belokurov, V., & Evans, N. W. 2022, *MNRAS*, 513, 5270
- Pérez Paolino, F., Bary, J. S., Petersen, M. S., et al. 2023, *ApJ*, 946, 10
- Petit, V., Owocki, S. P., Wade, G. A., et al. 2013, *MNRAS*, 429, 398
- Popinchalk, M., Faherty, J. K., Curtis, J. L., et al. 2023, *ApJ*, 945, 114
- Pribulla, T., Borkovits, T., Jayaraman, R., et al. 2023, *MNRAS*, 524, 4220
- Rajpurohit, A. S., Reylé, C., Allard, F., et al. 2013, *A&A*, 556, A15
- Rappaport, S., Barclay, T., DeVore, J., et al. 2014, *ApJ*, 784, 40
- Rappaport, S., Levine, A., Chiang, E., et al. 2012, *ApJ*, 752, 1
- Rappaport, S., Vanderburg, A., Jacobs, T., et al. 2018, *MNRAS*, 474, 1453
- Ratzenböck, S., Meingast, S., Alves, J., Möller, T., & Bomze, I. 2020, *A&A*, 639, A64
- Rebull, L. M., Stauffer, J. R., Cody, A. M., et al. 2018, *AJ*, 155, 196

- Rebull, L. M., Stauffer, J. R., Hillenbrand, L. A., et al. 2022, *AJ*, **164**, 80
- Rebull, L. M., Stauffer, J. R., Bouvier, J., et al. 2016, *AJ*, **152**, 114
- Reinhold, T., Bell, K. J., Kuszlewicz, J., Hekker, S., & Shapiro, A. I. 2019, *A&A*, **621**, A21
- Ricker, G. R., Winn, J. N., Vanderspek, R., et al. 2015, *Journal of Astronomical Telescopes, Instruments, and Systems*, **1**, 014003
- Rivinius, T., Carciofi, A. C., & Martayan, C. 2013, *A&A Rv*, **21**, 69
- Rizzuto, A. C., Newton, E. R., Mann, A. W., et al. 2020, *AJ*, **160**, 33
- Robinson, C. E., Espaillat, C. C., & Owen, J. E. 2021, *ApJ*, **908**, 16
- Rodriguez, D. R., van der Plas, G., Kastner, J. H., et al. 2015, *A&A*, **582**, L5
- Sanchis-Ojeda, R., Rappaport, S., Pallè, E., et al. 2015, *ApJ*, **812**, 112
- Sanderson, H., Jardine, M., Collier Cameron, A., Morin, J., & Donati, J. F. 2023, *MNRAS*, **518**, 4734
- Saur, J., Neubauer, F. M., Connerney, J. E. P., Zarka, P., & Kivelson, M. G. 2004, in *Jupiter. The Planet, Satellites and Magnetosphere*, ed. F. Bagenal, T. E. Dowling, & W. B. McKinnon, Vol. 1, 537
- Servén, D., & Brummitt, C. 2018, pyGAM: Generalized Additive Models in Python
- Skrutskie, M. F., Cutri, R. M., Stiening, R., et al. 2006, *AJ*, **131**, 1163
- Somers, G., Cao, L., & Pinsonneault, M. H. 2020, *ApJ*, **891**, 29
- Speagle, J. S. 2020, *MNRAS*, **493**, 3132
- Stassun, K. G., Kratter, K. M., Scholz, A., & Dupuy, T. J. 2012, *ApJ*, **756**, 47
- Stassun, K. G., Oelkers, R. J., Paegert, M., et al. 2019, *AJ*, **158**, 138
- Stauffer, J., Collier Cameron, A., Jardine, M., et al. 2017, *AJ*, **153**, 152
- Stauffer, J., Rebull, L., David, T. J., et al. 2018, *AJ*, **155**, 63
- Stellingwerf, R. F. 1978, *ApJ*, **224**, 953
- Townsend, R. H. D., & Owocki, S. P. 2005, *MNRAS*, **357**, 251
- Townsend, R. H. D., Owocki, S. P., & Groote, D. 2005, *ApJL*, **630**, L81
- Vanderburg, A., Johnson, J. A., Rappaport, S., et al. 2015, *Nature*, **526**, 546
- Vial, J.-C., & Engvold, O. 2015, *Astrophysics and Space Science Library*, Vol. 415, *Solar Prominences*
- Vines, J. I., & Jenkins, J. S. 2022, *MNRAS*, **513**, 2719
- Virtanen, P., Gommers, R., Oliphant, T. E., et al. 2020, *Nature Methods*, **17**, 261
- Vogt, S. S., Allen, S. L., Bigelow, B. C., et al. 1994, in *Society of Photo-Optical Instrumentation Engineers (SPIE) Conference Series*, Vol. 2198, *Instrumentation in Astronomy VIII*, ed. D. L. Crawford & E. R. Craine, 362
- Vos, J. M., Faherty, J. K., Gagné, J., et al. 2022, *ApJ*, **924**, 68
- Waugh, R. F. P., & Jardine, M. M. 2022, *MNRAS*, **514**, 5465
- Winters, J. G., Charbonneau, D., Henry, T. J., et al. 2021, *AJ*, **161**, 63
- Winters, J. G., Henry, T. J., Jao, W.-C., et al. 2019, *AJ*, **157**, 216
- Wright, E. L., Eisenhardt, P. R. M., Mainzer, A. K., et al. 2010, *AJ*, **140**, 1868
- York, D. G., Adelman, J., Anderson, John E., J., et al. 2000, *AJ*, **120**, 1579
- Zhan, Z., Günther, M. N., Rappaport, S., et al. 2019, *ApJ*, **876**, 127
- Zieba, S., Zwintz, K., Kenworthy, M. A., & Kennedy, G. M. 2019, *A&A*, **625**, L13
- Zuckerman, B. 2019, *ApJ*, **870**, 27
- Zuckerman, B., Bessell, M. S., Song, I., & Kim, S. 2006, *ApJL*, **649**, L115

Table 1. Bona fide, candidate, and debunked complex rotators from the TESS 2-minute data. For internal review, full versions are available here <https://www.dropbox.com/scl/fo/twn4s9ckbevf75jqhtoy1/h?rlkey=t5cn8cx2uoc2ptdm9e570kp1b&dl=0>

TIC –	<i>T</i> mag	<i>d</i> pc	$G_{\text{BP}} - G_{\text{RP}}$ mag	RUWE –	<i>P</i> hr	Assoc	Age Myr	T_{eff} K	R_* R_{\odot}	M_* M_{\odot}	R_c R_*	P_{sec} hr	Quality –	Bin –	N_{sector} –
368129164	9.29	18.3	2.89	6.95	6.44	ABDMG	149	3140	0.71	0.4	1.81	2.60	1	011	3
405754448	9.63	92.6	1.75	6.81	12.92	LCC	15	4273	1.5	0.82	1.74	134.4	1	011	5
167664935	10.31	62.5	2.52	5.05	14.05	UCL	16	3325	1.42	0.38	1.5	10.71	1	011	3
311092148	11.03	26.8	3.03	1.5	7.86	COL	42	3035	0.5	0.27	2.6	–	1	000	1
402980664	11.11	21.3	3.04	1.48	18.56	COL	42	3080	0.37	0.22	5.76	–	1	000	10
50745567	11.28	38.0	3.22	3.95	6.34	BPMG	24	3014	0.67	0.28	1.68	28.55	1	011	2
59836633	11.38	61.9	2.71	1.21	14.96	BPMG	24	3282	0.82	0.48	2.91	–	1	000	3
425933644	11.4	43.2	2.82	10.29	11.67	THA	45	3151	0.63	0.4	3.06	–	1	010	6
142173958	11.61	70.6	3.09	2.9	11.76	TWA	10	3028	1.15	0.26	1.45	12.84	1	011	3
146539195	11.62	48.2	3.37	2.86	6.73	BPMG	24	2898	0.8	0.24	1.38	7.29	1	011	2
206544316	11.63	42.8	2.89	1.26	7.73	THA	45	3114	0.57	0.35	2.44	–	1	000	6
335598085	11.9	105.5	2.85	2.79	15.85	LCC	15	3119	1.34	0.28	1.56	17.94	1	011	3
405910546	12.11	111.9	2.36	1.09	37.99	LCC	15	3455	0.92	0.6	5.26	–	1	100	4
272248916	12.15	80.5	2.83	5.5	8.9	UCL	16	3193	0.81	0.4	1.97	50.7	1	011	3
178155030	12.17	46.8	2.91	1.29	11.67	THA	45	3097	0.49	0.3	3.53	–	1	000	4
224283342	12.29	38.0	3.04	1.27	21.3	COL	42	3050	0.39	0.22	6.08	–	1	100	3
89026133	12.31	131.6	2.82	4.0	11.2	UCL	16	3188	1.33	0.31	1.29	27.83	1	011	3
234295610	12.51	48.1	3.04	1.13	18.29	THA	45	3074	0.44	0.27	5.09	–	1	000	3
118449916	12.54	97.1	3.09	25.18	12.31	TAU	2	3025	1.04	0.28	1.7	6.71	1	011	4
67897871	12.55	148.2	3.01	2.55	6.23	USCO	10	3082	1.5	0.18	0.65	6.72	1	011	2
353730181	12.65	106.6	2.75	1.23	13.51	TAU	2	3253	0.8	0.41	2.65	–	1	000	4
201898222	12.68	42.2	3.21	1.29	10.7	THA	45	2996	0.39	0.2	3.69	13.62	1	001	5
264767454	12.73	123.3	2.93	12.3	10.01	COL(?)	42	3150	1.0	0.42	1.76	20.62	1	011	13
442571495	12.75	80.8	3.03	1.64	9.59	UCL	16	3099	0.65	0.3	2.35	13.82	1	001	3
2234692	12.8	53.7	3.0	1.2	6.52	COL	42	3098	0.44	0.26	2.56	59.8	1	001	7
94088626	12.88	57.6	3.07	1.12	6.6	ARG	45	3090	0.46	0.27	2.53	–	1	000	2
264599508	12.88	79.7	3.01	1.89	7.9	COL	42	3098	0.62	0.4	2.4	8.99	1	001	7
363963079	12.92	83.1	3.09	8.0	7.82	ARG	45	3040	0.67	0.4	2.21	7.41	1	011	7
193831684	13.03	51.6	3.23	1.16	31.02	BPMG	24	2971	0.42	0.2	6.87	–	1	000	3
177309964	13.1	91.0	2.94	1.15	10.88	CAR	45	3125	0.62	0.4	2.95	–	1	000	34
425937691	13.18	43.1	3.77	2.86	4.82	THA	45	2782	0.41	0.16	1.91	3.22	1	011	5
141146667	13.28	57.6	3.28	1.23	3.93	FIELD	NaN	2968	0.42	NaN	NaN	–	1	000	6
332517282	13.29	39.0	3.27	1.05	9.67	ABDMG	149	2975	0.28	0.2	4.87	–	1	000	3
144486786	13.3	77.4	3.05	15.05	6.82	COL	42	3074	0.51	0.3	2.38	11.49	1	011	4
38820496	13.3	44.1	3.37	1.08	15.73	THA	45	2903	0.34	0.16	5.13	–	1	000	5
289840926	13.31	40.2	3.75	1.16	4.8	BPMG	24	2807	0.36	0.14	2.05	15.64	1	001	3
404144841	13.33	77.1	3.19	1.11	10.74	TWA	10	3008	0.52	0.22	2.86	–	1	000	4
89463560	13.45	123.9	2.97	1.31	9.43	ARG	45	3055	0.75	0.37	2.15	7.76	1	001	10
300651846	13.49	109.2	2.86	1.16	8.26	CAR	45	3136	0.62	0.4	2.44	–	1	000	31
267953787	13.49	130.5	3.59	1.2	17.46	TAU	2	2826	1.06	0.12	1.59	–	1	000	4
68812630	13.6	123.8	3.22	1.63	9.04	TAU	2	2996	0.76	0.27	1.86	5.28	1	001	3
141306513	13.65	50.2	3.4	1.08	13.36	THA	45	2964	0.32	0.16	4.85	–	1	000	2
201789285	14.03	45.4	3.82	1.19	3.64	THA	45	2757	0.3	0.12	2.02	–	1	000	5
294328887	14.23	97.1	3.22	1.05	8.51	CARN	200	2994	0.45	0.35	3.33	–	1	000	35

Table 1 *continued*

Table 1 (*continued*)

312410638	14.3	136.9	3.12	1.09	28.06	UCL	16	3030	0.58	0.25	5.11	-	1	000	3
38539720	14.52	129.4	3.37	1.2	9.16	PERI	120	2924	0.57	0.25	2.43	-	1	000	1
359892714	14.53	95.5	4.04	1.07	11.33	EPSC	3	2675	0.55	0.13	2.36	-	1	000	6
118769116	14.58	119.0	3.6	1.13	8.56	TAU	2	2852	0.56	0.2	2.18	-	1	000	4
440725886	14.69	135.1	2.96	1.06	3.92	PLE	112	3109	0.45	0.35	1.99	-	1	000	5
397791443	15.01	151.1	3.1	1.06	6.95	IC2602	46	3031	0.48	0.26	2.46	-	1	000	6
160329609	9.65	8.7	3.4	1.18	24.31	ARG	45	2912	0.35	0.16	6.6	-	0	000	3
148646689	12.14	140.4	2.44	1.7	10.63	UCL	16	3466	1.25	0.55	1.61	13.37	0	001	3
280945693	12.27	98.2	2.97	1.16	15.27	LCC	15	3103	1.09	0.31	1.94	-	0	100	5
165184400	12.37	43.2	3.02	1.24	15.91	THA	45	3076	0.42	0.25	4.74	-	0	000	4
245834739	12.55	115.4	2.85	1.49	10.47	TAU	2	3112	1.02	0.36	1.68	9.86	0	001	6
125843782	13.01	127.7	2.86	1.21	44.17	TAU	2	3135	0.9	0.35	4.97	-	0	000	4
244161191	13.17	44.7	3.54	1.28	7.17	COL	42	2860	0.38	0.18	2.8	8.39	0	001	3
231058925	13.17	51.2	3.25	1.35	8.87	THA	45	2978	0.38	0.2	3.33	-	0	000	5
301676454	13.4	70.7	3.07	1.24	9.18	ARG	45	3009	0.47	0.25	2.96	-	0	000	1
58084670	13.58	140.2	2.82	1.06	11.16	FIELD	NaN	3138	0.77	NaN	NaN	-	0	000	6
67745212	13.63	27.8	3.8	1.11	5.12	COL	42	2781	0.21	0.09	3.17	-	0	000	2
5714469	13.73	78.3	3.65	1.12	10.35	UCL	16	2828	0.54	0.18	2.53	-	0	000	3
259586708	13.82	95.6	2.93	1.17	22.52	COL	42	3133	0.46	0.29	5.84	-	0	000	7
435903839	11.95	80.7	2.49	17.7	10.82	ABDMG(?)	149	3458	0.76	0.54	2.66	-	-1	010	6
57830249	11.96	48.8	3.2	1.34	43.82	TWA	10	2948	0.7	0.25	5.63	-	-1	000	3
193136669	13.06	61.1	3.49	1.22	37.64	TWA	10	2855	0.58	0.19	5.62	-	-1	000	4

NOTE—This table includes 50 good CRs (Quality flag 1), 13 ambiguous CRs (Quality flag 0), and 3 impostors (Quality flag -1). The three-bit binarity flag “Bin” is for Gaia DR3 `radial_velocity_error` outliers (bit 1), Gaia DR3 `ruwe` outliers (bit 2), and stars with multiple TESS periods (bit 3). The machine-readable version, available online, includes additional columns for the Gaia DR2 and DR3 source identifiers, as well as the stellar parameter uncertainties. The age uncertainties are typically $\approx \pm 10\%$, but can be asymmetric. The median statistical uncertainties on the temperature, radius, and mass are $\pm 50\text{ K}$, $\pm 4\%$ and $\pm 9\%$ respectively. N_{sector} denotes the number of TESS sectors for which *any* data are expected to be acquired between July 2018 and Oct 2024. This number is generally greater than the number of sectors for which 120-second cadence data exist. Association names and provenance follow conventions adopted by Gagné et al. (2018): ABDMG: AB Doradus moving group (Bell et al. 2015). ARG: Argus (Zuckerman 2019). BPMG: β Pic moving group (Bell et al. 2015). CARN: Carina Near moving group (Zuckerman et al. 2006). COL: Columba (Bell et al. 2015). EPSC: ϵ Chamæleonis (Murphy et al. 2013). LCC: Lower Centaurus Crux (Pecaut & Mamajek 2016). PERI: Pisces-Eridani (Curtis et al. 2019). PLE: Pleiades (Dahm 2015). TAU: Taurus (Kenyon & Hartmann 1995). THA: Tucana-Horologium association (Bell et al. 2015). TWA: TW Hydriæ association (Bell et al. 2015). UCL: Upper Centaurus Lupus (Pecaut & Mamajek 2016). USCO: Upper Scorpius (Pecaut & Mamajek 2016). The “(?)” string denotes low-confidence membership.

APPENDIX

A. THE RING HYPOTHESIS

One hypothesis for the CRs, presented by Zhan et al. (2019), is that the star might be “*orbited by one or more rings composed of dust-size or somewhat larger particles... The ring particles would move in Keplerian orbits at relatively large distances from the star, and therefore the sublimation lifetime would not be an issue even if the particles are dust-like in size.*” A sketch of this scenario was presented by Zhan et al. (2019), in their Figure 11. An example set of proposed parameters involved a ring inclined with respect to the stellar spin axis by a few degrees, and with inner and outer radii of 10 and 15 stellar radii.

One concern with the ring hypothesis is that if a cool spot were to transit behind the ring, it would produce a brightening, not a dimming. Most CRs show dimmings. The ring scenario would therefore imply that large hot spots are common in the photospheres of pre-main-sequence M dwarfs. Empirical evidence however suggests that cool spots dominate the the optical variability of disk-free pre-main-sequence stars. This evidence includes flux excursions caused by spot-crossings during planetary transits (e.g. Rizzuto et al. 2020; Gilbert et al. 2022), correlations between simultaneous photometric and chromospheric time-series (Reinhold et al. 2019), and stellar spectra that show molecules that only form at cool temperatures (e.g. Gully-Santiago et al. 2017; Pérez Paolino et al. 2023).

An independent concern with the ring hypothesis is that it is fine-tuned. The model requires specific locations for the inner edge and the outer edge of the ring, an inclination that yields a band with a specific apparent size, and material in the ring that must be optically thick while also being homogeneous enough to not induce any apparent photometric variability. It is challenging

to ascribe specific probabilities to any one of these factors. However the requirement that they all be simultaneously met seems sufficiently severe to disfavor this scenario.

B. TIC 300651846

Figures 11 and 12 show 120-second cadence data for TIC 300651846, a CR in the TESS continuous viewing zone. If it were not for the existence of TIC 402980664, this source would have received greater attention. With the exception of a few sectors, TESS data will exist for TIC 300651846 for at least Sectors 1-12, 27-39, and 61-69. While most of the available data exist in the full frame images, Figures 11 and 12 focus only on the currently available 120-second cadence data.

During Sectors 32-39, the source shows between one and four local minima per cycle. During the early portions of Sectors 61-65, it is more complex, with at least five clear local minima per cycle. As the source evolves, its shape becomes simpler, and the sharpness of one global minimum appears to increase.

State-switches analogous to those observed in LP 12-502 occur at cycles 498 and 2554. During the cycle 498 switch, two narrow dips at $\phi \approx -0.4$ and $\phi \approx 0.0$ collapse. For the cycle 2554 switch, a longer dip collapses. This is visible as a change in curvature in Figure 11 between $\phi \in [-0.25, -0.05]$ across cycles 2520-2561. The more typical dip evolution timescales for TIC 300651846 seem to be $\approx 50\text{-}100$ cycles. Unlike the TIC 402980664 river plots (Figure 9), we did not subtract any “continuum sinusoid” for this source, because the continuum is not as obviously defined.

C. NO SIGNIFICANT POWER AT 20 SECOND CADENCE

TESS was the first instrument to show that CR light curves contain power at timescales of a few minutes (Zhan et al. 2019; Günther et al. 2022). This advance was enabled by the fifteen-fold faster cadence in the TESS 2-minute data, relative to K2. A logical follow-up is to ask whether the periodic components of the CR light curves contain power at timescales below one minute. Between 2020 and 2021, we observed 10 CRs at 20-second cadence with TESS in order to explore this question (TESS DDT029; PI L. Bouma). The stars were TICs 142173958, 146539195, 24518895, 276453848, 264599508, 363963079, 144486786, 408188366, 300651846, 262400835. These sources were selected from CRs known at the time to have short periods and sharp features when observed at 2-minute cadence. Comparing the 20-second to 120-second data for these stars (data available on MAST), we concluded that these CRs did not contain appreciable power at timescales shorter than a few minutes.

D. THE CRS ARE NOT OBVIOUSLY ACCRETING

We acquired iodine-free reconnaissance spectra using Keck/HIRES for three CRs. The goals were to determine the chromospheric activity levels, and to check for indications of either accretion or spectroscopic binarity. We acquired a 15 minute exposure of TIC 146539195 on 2023 January 3, a 15 minute exposure of TIC 264599508 on 2023 January 9, and a 30 minute exposure of TIC 402980664 on 2023 July 10. The acquisition and analysis followed the usual techniques of the California Planet Survey (Howard et al. 2010). Figure 13 shows cutouts from the resulting spectra, centered on the Ca II HK windows, H α , and the Li I 6708 Å doublet. The Ca II H emission line is blended with He. While a more detailed analysis will be left for future work, these spectra confirm previous understanding established by Stauffer et al. (2017) that the stars are chromospherically active M dwarfs in the “weak-lined” T Tauri regime (e.g. Briceño et al. 2019, Figure 15). Their H α equivalent widths, at ≈ 14 Å, ≈ 3 Å, and ≈ 8 Å (for TIC 264599508, 146539195, and 402980664 respectively) are consistent with purely chromospheric emission. The blue excess in TIC 264599508 could be explained by a second unresolved star; the TESS light curve for this source shows both the 7.90 hr CR signal, and a 9.00 hr rotation signal with comparable amplitude.

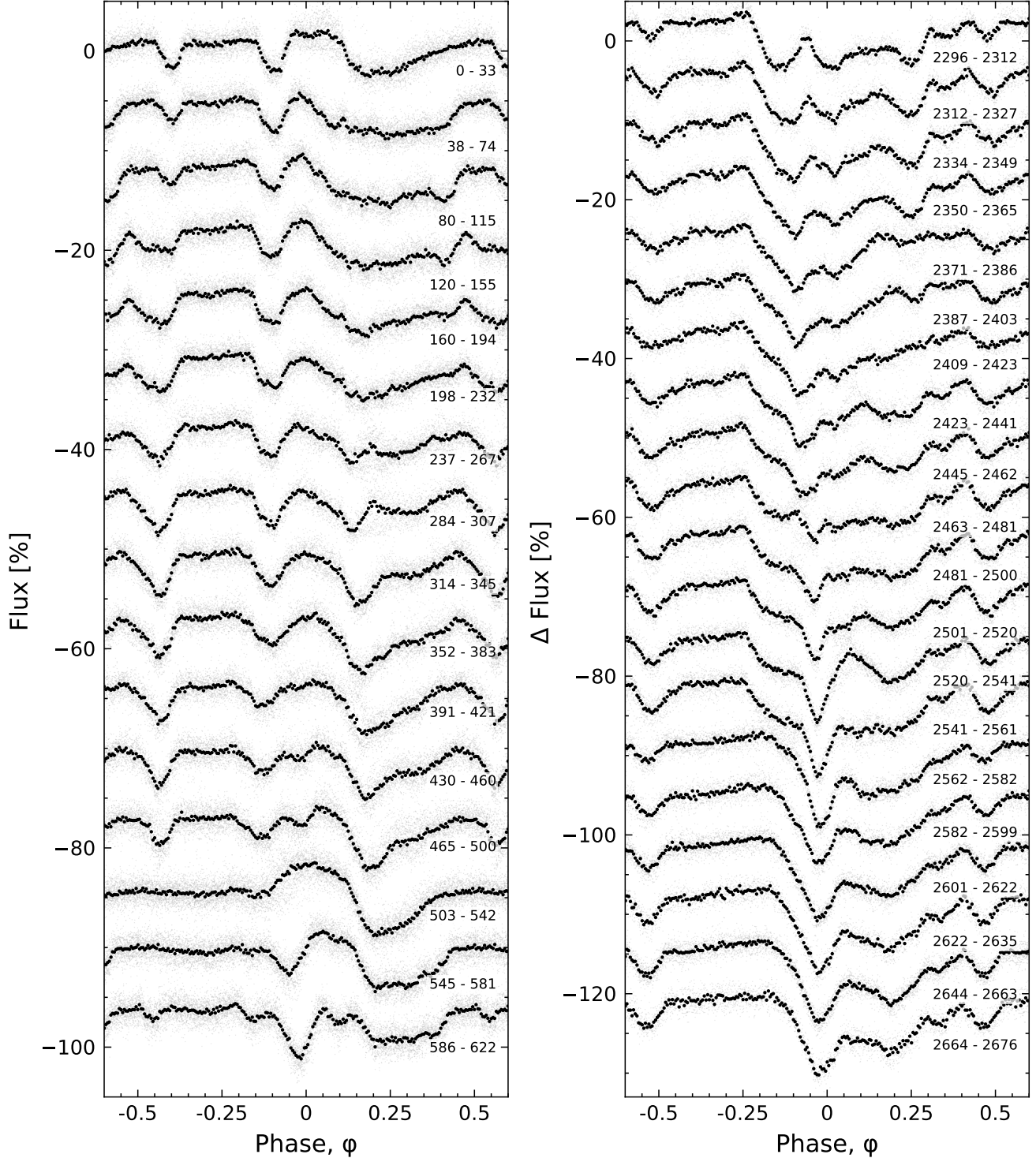


Figure 11. Light curve evolution of TIC 300651846. All available 120-second cadence data as of 2023 Aug 11 are shown. Cycles 0 to 622 span TESS Sectors 32-39 (Nov 2020–June 2021); cycles 2296-2676 span Sectors 61-65 (Jan–June 2023). We assumed a 8.254 hr period and a fixed reference epoch (BTJD 2174.127) for both panels. Light curve segments are split based on the presence of gaps longer than three hours. Cycle numbers are listed in the lower-right of each light curve segment.



Figure 12. River plots of TIC 300651846. This is an alternative visualization of the data in Figure 11. All available 120-second cadence data as of 2023 Aug 11 are shown. Cycles 0 to 622 span TESS Sectors 32-39 (Nov 2020–June 2021); cycles 2296-2676 span Sectors 61-65 (Jan–June 2023). We assumed $P=8.254$ hr and $t_0=2174.127$ [BTJD]. Note that the two panels have slightly different color scales.

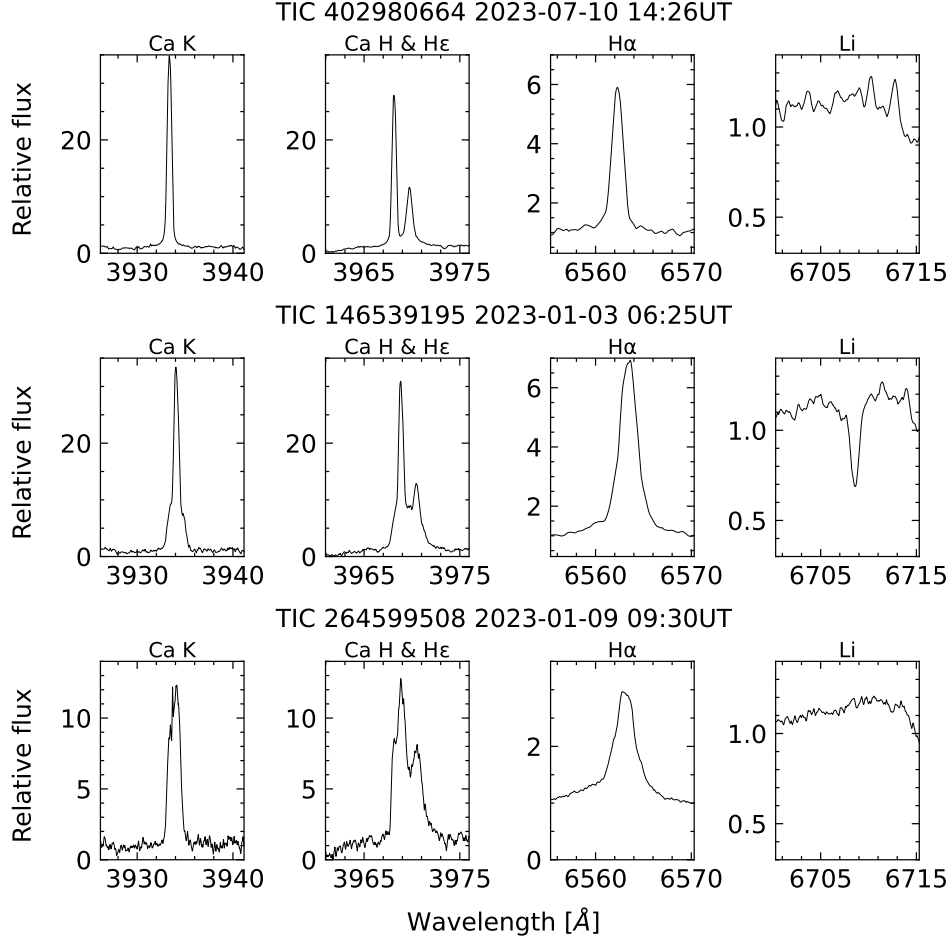


Figure 13. Spectral age and activity diagnostics for three CRs. Wavelengths are in air; the continuum normalization is relative to the entire order. The H α emission strength classifies the stars as weak-lined T Tauris. The lithium detection for TIC 146539195 is consistent with its mass and β Pic membership; the non-detections for TIC 402980664 and TIC 264599508 are consistent with the \approx 42 Myr age implied by their membership in the Columba moving group.